Tri-Suction Pile Caisson

Analysis of Soil-Structure Interaction

Evangelos Christantonis

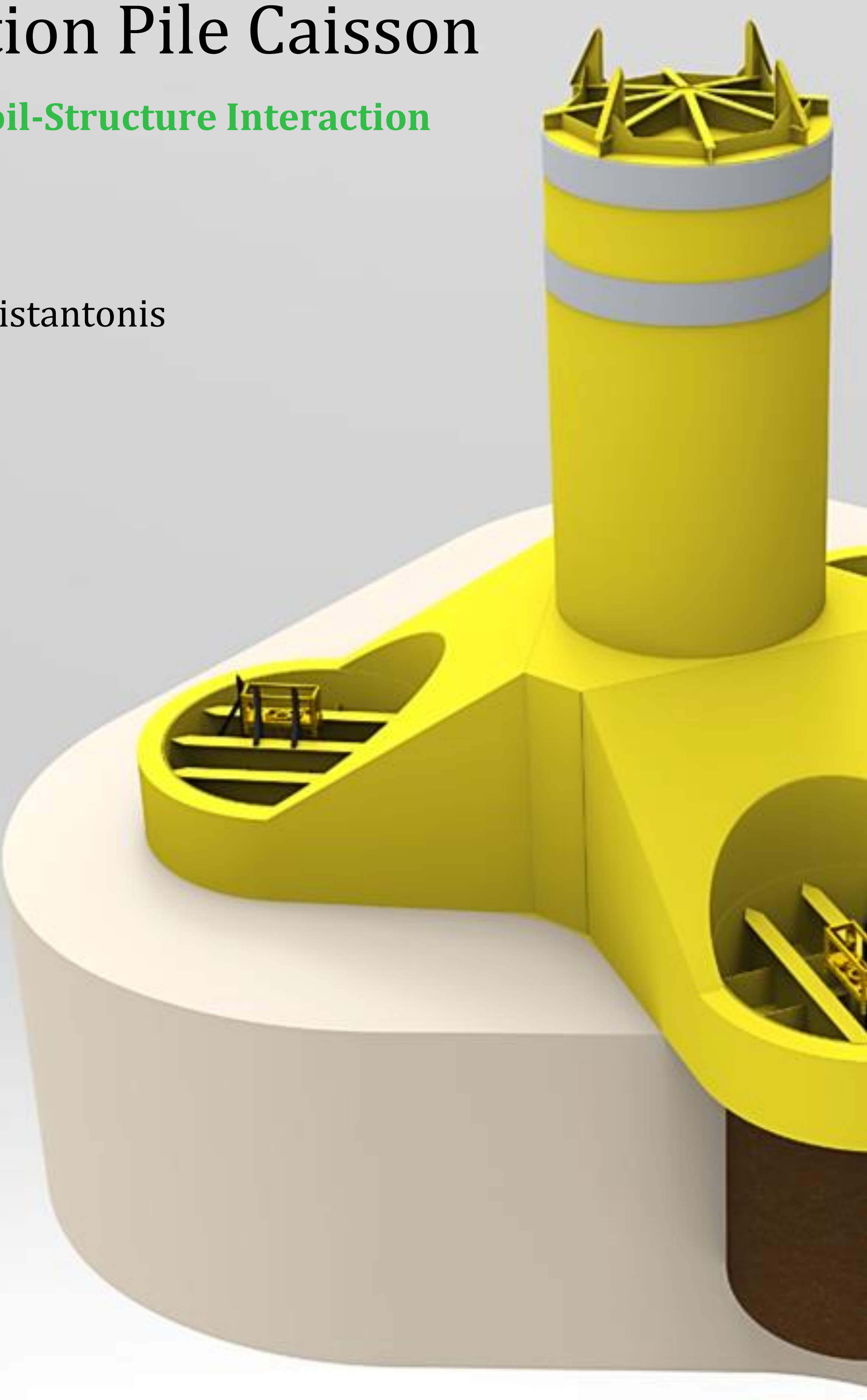

Tri-Suction Pile Caisson

Analysis of Soil-Structure Interaction

by

Evangelos Christantonis

To obtain the degree of Master of Science in

Offshore and Dredging Engineering at Delft University of Technology

To be defended publicly on Thursday February 17, 2022 at 16:00 h

Committee:	Prof. Dr. Ir. A. Metrikine	TU Delft	Chairman
	Dr. Ir. B. Ummels	TU Delft	Supervisor
	J. A. Rebollo Parada	SPT Offshore	Supervisor

Abstract

Offshore wind turbines are getting larger and are being installed in ever deeper waters. This requires increasingly stronger yet affordable foundations. The Tri-Suction Pile Caisson (TSPC) is a Wind Turbine Generator (WTG) foundation concept patented by SPT Offshore that requires a smaller amount of structural steel or concrete than a conventional monopile. It can be towed from port to location, and can, thus, be installed by smaller crane vessels. Additionally, it does not require piledriving or noise mitigation measures. Despite its promising potential, unlike its competitors and proven technologies, i.e., the monopile and the Suction Bucket Jacket (SBJ), little is known about the in-place behaviour of the TSPC in sandy or clayey soil types.

This study aims to further existing knowledge regarding the interaction between the three clustered suction piles and the surrounding soil and, subsequently, contribute towards making the TSPC an economically feasible option. To this end, a parametric analysis was conducted using PLAXIS 3D, a Finite Element Modelling (FEM) software, to assess the effect of suction pile centre-to-centre distance, load combination and soil type on the TSPC behaviour under monotonic static loading.

To validate computational results against realistic values, the calculation of the environmental loads acting on the TSPC and the soil constitutive model parameters calibration were made using metocean and geotechnical data from the Aberdeen Offshore Wind Farm (AOWF).

In total, five centre-to-centre distances were considered ranging from 1.2 to 2.0 times the diameter of the suction buckets. Two governing Ultimate Limit State (ULS) load combinations were identified, corresponding to WTG rated wind speed and 50-year storm conditions. Finally, two soil types were addressed, medium-loose sand, modelled by the Hardening Soil Model (HSM) and soft-stiff clay, represented by the NGI-ADP model. The contribution of the above parameters to the mobilization of failure mechanisms, and the evolution of foundation stiffness, was investigated.

Based on this work, it is concluded that the TSPC behaves very similarly to a mono-caisson for the most clustered geometrical configurations, especially in clay, where the formation of an inner soil plug is evident. For larger centre-to-centre distances in sandy soils, the TSPC approaches the behaviour of the SBJ, with the mobilization of axial caisson pair capacity being the main resistance factor against overturning moment loading. With the current knowledge, it is not straightforward to determine which geometrical configuration is the most optimal in terms of structural steel efficiency and installability in sand and clay. Thus, the challenge of the TSPC design optimization remains.

The results of this work, however, can be used to outline the optimization process by providing starting points for normalised centre-to-centre distances in sand and clay, combined with further research on the quantification and normalisation of connection beam costs and rigidity. The investigation of different embedment ratios, accounting for installability, would also contribute to that direction. Finally, the assessment of TSPC behaviour under cyclic and dynamic load is encouraged since it can shed light on a potential strategic advantage against conventional WTG foundations.

Preface

This master thesis is the conclusive requirement in the Offshore & Dredging Engineering Master Programme of TU Delft and, in all likelihood, means the end of my academic journey. Being a keen sailor, I am inclined to look abaft as well as ahead, thus, before I embark on my next voyage aboard SPT Offshore, I feel the urge to thank those that equipped me with the tools to do so:

First and foremost, I would like to thank Bart Ummels, my TU Delft supervisor, for his consistent commitment to motivating and providing me with invaluable mental and practical support, that helped me punch through the highs and lows of this thesis.

I am also very thankful towards Juan A. Rebollo Parada, my SPT Offshore supervisor, for managing to endure my volleys of questions related to soil engineering and suction piles. I would also like to thank Erik ter Horst for ensuring my timely exposure to technical documentation and design principles.

I must also thank the committee chairman, Professor Andrei Metrikine, for his simple, yet challenging questions during our progress meetings, that ensured I have a proper grasp of the fundamental concepts in my thesis project.

Finally, I am inexplicably grateful towards my family, especially my mother, a fellow engineer, who, thankfully, failed to turn me into a doctor; my partner Elli for her unconditional support and of course, my friends for making this effort worthwhile.

Evangelos Christantonis,

Delft, February 2022

If you can't convince them, confuse them. - Unknown

Contents

List of Figures

List of Tables

List of Acronyms

ALS	Accidental Limit State
AOWF	Aberdeen Offshore Wind Farm
CAPEX	Capital Expenditure
DLC	Design Load Case
DNV	Det Norske Veritas
EOWDC	European Offshore Wind Deployment Centre
FEM	Finite Element Modelling
FLS	Fatigue Limit State
HAT	Highest Astronomical Tide
LAT	Lowest Astronomical Tide
LCOE	Levelized Cost of Energy
LRFD	Load Resistance Factor Design
MSL	Mean Sea Level
NFA	Natural Frequency Analysis
OPEX	Operating Expense
OWF	Offshore Wind Farm
RNA	Rotor Nacelle Assembly
SI	ISO International System of Units
SLS	Serviceability Limit State
TSPC	Tri Suction Pile Caisson
ULS	Ultimate Limit State
WTG	Wind Turbine Generator

1. Introduction

1.1 The State of Offshore Wind

Windmills are rumoured to have existed in the Middle East since the 7th century, however, they did not see widespread use in Europe until the Middle Ages. Down the line, either being used in agriculture for corn or wheat grinding or assaulted by the brave Don Quixote in the Cervantes universe, windmills evolved throughout the centuries into their formidable offspring, the wind turbines. As energy demands grow bigger and fossil fuels fail to secure a sustainable and environmentally friendly energy future, more and more country governments are turning their attention to renewables, with wind energy playing a major role in that transition. The first wind turbine was built in Scotland by Professor James Blyth in 1887. Relatively recently, due to spatial limitations onshore, visual, and acoustic pollution, upscaling purposes, as well as favourable wind potential at sea, the blooming wind industry is witnessing a shift to offshore projects with the first offshore wind farm developed in Vindeby, Denmark, in 1991.

Europe led the way in this transition, given the abundant wind potential and shallow water depth of the North Sea, corresponding to 94.6% of globally offshore installed capacity by 2015 (IRENA, 2021). However, as wind energy harvesting becomes more and more innovative, the feasibility spectrum is expanding and new players are entering the competition, with China corresponding to 26.5% of the 34.4 GW offshore installed capacity worldwide as of 2020 (IRENA, 2021). More recently, under the new administration, the United States has also entered the race, being forecast to install more offshore wind capacity in 2024 than any other country in the world, resulting in more than 5 GW by 2025 (IEA, 2020). Figure 1-1 shows the growing trend in offshore wind capacity additions worldwide, which are expected to reach a record 8.8 GW in 2022, led by China and the United Kingdom, corresponding to almost 15% of total wind additions, 50% higher than in 2019 (IEA, 2020).

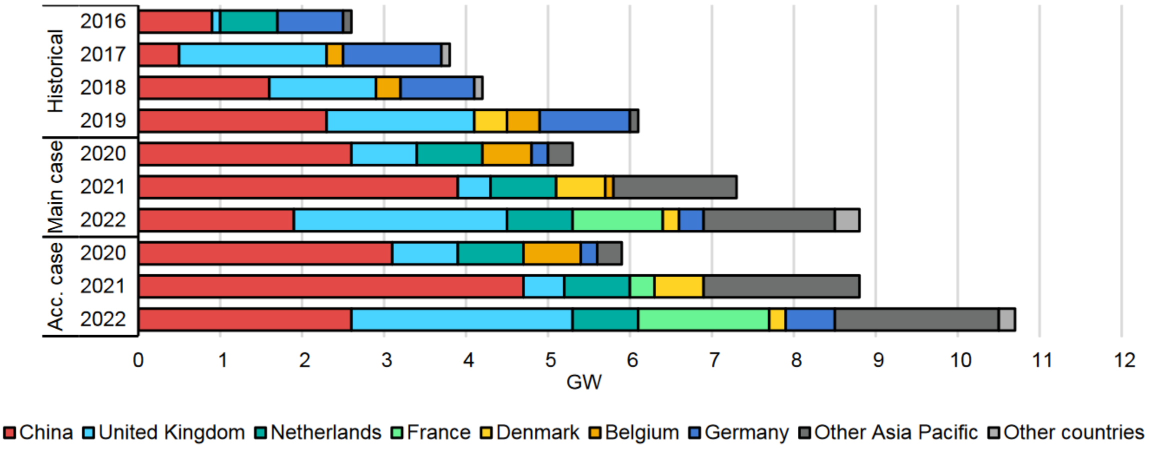

Figure 1-1 Offshore wind net capacity additions by country/region (IEA, 2020).

With efficiency and lower levelized cost of energy (LCOE) being the driving factor for offshore wind, the industry is following a trend to larger wind turbines with an average rated capacity of 5.5 MW in 2018, which is projected up to 12.0 MW in 2025 (IRENA, 2019), while in Europe the average capacity was 6.8 MW and 7.8 MW for 2018 and 2019, respectively. Stepping into the future, major OWT manufacturers are participating in the upscaling race with General Electric taking the initiative since Haliade-X is already set to be used in the Dogger Bank wind farm, with construction expected to begin in 2022. With a rotor diameter of 220 m, it can provide an output from 12 MW to 14 MW with a 60-

64% capacity factor (GE Renewable Energy, 2021). In addition, Siemens Gamesa has announced the production of the SG 14-222 DD 14 MW turbine with a rotor diameter of 222 m and potential capacity expansion of up to 15 MW (Siemens Gamesa, 2021). Following the trend, Vestas has introduced their V236 turbine at 15 MW and 236 m rotor diameter, with a capacity factor of over 60% (Vestas, 2021). Finally, MingYang Smart Energy is intending to break the competition with the MySE 16.0-242, featuring 16 MW of nominal capacity and 242 m rotor diameter, which is expected to hit production by the first half of 2024 (MingYang Smart Energy, 2021).

The average size of wind farms has also increased with a European average of 621 MW (WindEurope, 2019) with the trend in Europe being for projects of over 1000 MW of installed capacity (Hornsea, Dogger Bank, Hollandse Kust). Moreover, the consequent smaller number of wind turbines for a given wind farm capacity, leads to fewer individual foundations, shorter installation, and fewer maintenance visits that correspond to lower capital (CAPEX) and operational (OPEX) costs. As a result, the levelized cost of energy (LCOE) for offshore wind has dropped from USD 160/MWh in 2010, to USD 130/MWh in 2018 (IRENA, 2019). In 2021, the average LCOE for bottom founded offshore wind installations dropped further, to USD 95/MWh, with predictions of approximately USD 56/MWh by 2030 (US Department of Energy, 2021). Similar prices have been observed in the EU already at selected locations in Germany and the Netherlands, although these costs do not include grid connection to shore.

The upscaling tendency in turbine capacity, the future saturation of shallow water areas, as well as the expansion of the offshore wind market in countries like the United States or Japan, where a considerable part of the wind potential is in mid-ranged or larger water depths (Figure 1-2), create a new challenge and need for innovation in wind turbine support structure design. Figure 1-3 provides an overview of announced and operational projects. Water depths between 30-40 m are already the norm, while new projects are being announced for depths ranging from 40-75 m. In 2020 the LCOE for floating solutions was at USD 160/MWh, matching the bottom founded standards from 10 years ago, and is estimated to drop to USD 60-105/MWh by 2030 (US Department of Energy, 2021). Consequently, an extension of the feasibility range of bottom founded solutions might be necessary to bridge the gap of intermediate water depths until floating offshore wind is competitive.

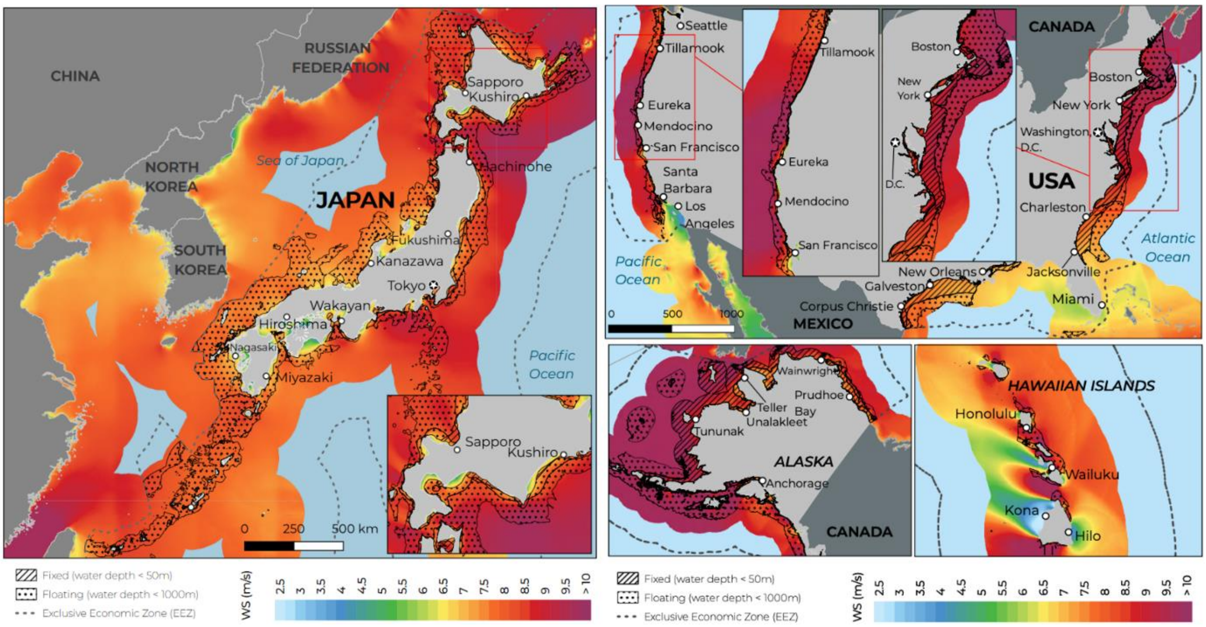

Figure 1-2 Wind potential and concept feasibility in Japan and the United States (ESMAP, 2021).

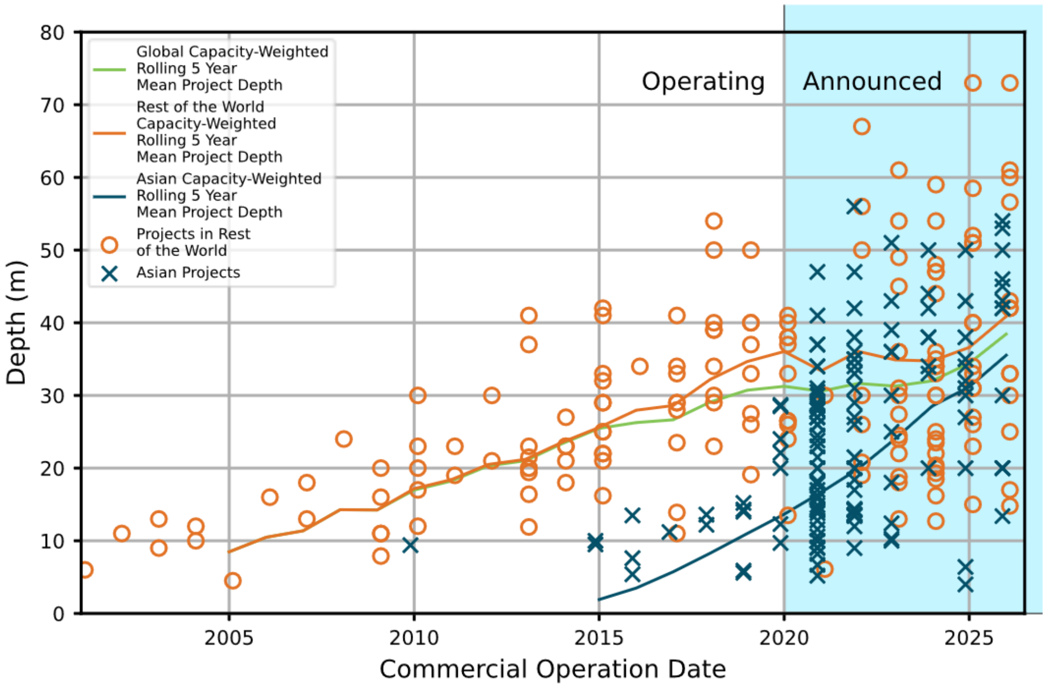

Figure 1-3 Offshore wind global project water depth (US Department of Energy, 2021).

1.2 Conventional Foundations for OWT

1.2.1 Monopile

Traditionally, the offshore wind industry has greatly favoured the monopile, which as of 2020 represents 74.8% of the total installed offshore wind foundation market (US Department of Energy, 2021). The main advantage of the monopile is its low cost, in terms of fabrication (low-cost steel, fast manufacturing), transportation (convenient shape, horizontal positioning on deck) and simple installation. Due to its popularity and extensive track record, there is abundant operational experience and research around the monopile, that allows the industry to push its feasibility limits above what has been considered the threshold of 40 meters water depth (Damiani et al., 2016). However, the market's shift towards larger WTG and water depths, and thus, larger monopile diameters and lengths, remains challenging. For example, fabrication feasibility of increasing D/t ratios, monopile integrity during transportation (local stresses and plasticity at supports), vessel size and hammer capacity limitations, installation feasibility (pile-driving fatigue, local buckling, noise mitigation) and monopile natural frequencies approaching the peaks of wave spectra, pose new challenges (Empire Engineering, 2020; Liu, 2021).

1.2.2 Jacket Structures

The second most prevalent foundation choice for offshore wind are jacket structures, representing 10.8% of existing projects as of 2020 e.g., Aberdeen OWF and Beatrice OWF (US Department of Energy, 2021) and 20% of the global announced market e.g., East Anglia ONE and Moray East (Offshore magazine, 2020). In certain water depths, they can overlap with monopile solutions but are currently the dominant choice for projects above 40 meters (Damiani et al., 2016). Jackets are foundations that use a lattice framework, and which usually have three or four anchors (slender piles or suction caissons) set on the seafloor. They take advantage of their spatial structural behaviour and slender members (smaller projected area and hydrodynamic drag) to sustain large moment and shear loads, and due to their extensive use in the oil and gas industry, there is wide experience around their design and maintenance. Their biggest disadvantage is their cost, both in terms of procurement and design (high-cost steel) and transportation/installation (large size, limited modularity) (Lozano-Minguez et al., 2011).

1.2.3 Gravity Based

Gravity based offshore wind foundations (GBS) are concrete structures that use gravel, sand, or stone ballast and base area to provide sufficient counter moment. They make use of prestressed steel for tensile capacity and most often require a gravel bed between soil and structure. GBS have fallen in popularity recently as projects steer away from shallow waters (above 30 m) (Oh et al., 2018), with their market share (number of foundations) dropping from 25% in 2010 to 10.4% in 2015 (Carbon Trust, 2015), however, alternative concepts of GBS can be adapted for deeper waters. They are, like jackets, proven technology and use low-cost materials (e.g., concrete). Another advantage is potential tugboat transportation on-site and the omission of crane installation. However, the extensive preparation of the seabed (dredging) and their large footprint have a significant environmental impact. Examples of GBS concepts in offshore wind are Nysted / Rødsand 1&2 and Lillgrund.

1.2.4 Tripods

Tripod foundations usually refer to three-legged bases connected to a cylindrical central column below the waterline (not to be confused with tri-pile foundations, where three individual pile legs connect to a central support tower above the waterline, e.g., Bard Offshore 1. They have very limited use in the offshore wind industry so far, 3.2% of total installed capacity (e.g., Alpha Ventus OWF, Global Tech 1 OWF) as of 2020 (US Department of Energy, 2021), mainly because they have the same application range as jackets. However, despite lacking a notable track record, they might offer certain advantages over monopiles and jackets for intermediate water depths (Lozano-Minguez et al., 2011). It is a much sturdier structure compared to the monopile, using spatial behaviour, but potentially simpler and cheaper to manufacture and transport than the jacket. Finally, the tripod legs can be supported either by suction caissons or skirt piles.

1.2.5 Suction Pile Foundations

Suction installed units are hollow cylindrical steel structures with an open bottom (reversed buckets) and their installation takes advantage of a hydraulically controlled pressure differential between the inside and outside of the bucket. The same general concept is used in sandy and clayey soils, with high and low permeability, respectively, but with different limitations and acting geotechnical mechanisms (Houlsby & Byrne, 2005a; Houlsby & Byrne, 2005b). Suction assisted installation, is a fast, controlled, silent and reversible process, that allows for shorter time offshore, easily achievable tilt restrictions, zero need for noise mitigation and full decommissioning at the end of the project lifetime (Oh et al., 2018). Their major disadvantage is their sensitivity to geohazards during installation, e.g., piping, soil plug heave, uneven mudline, or boulders, that require specific pre-emptive or reacting mitigation measures (Sturm, 2017).

1.3 The Next Step

As explained in sector 1.1, the offshore wind industry trend is governed by upscaling. The tendency is towards larger WTG, with longer blades and higher nominal power, resulting in higher hub heights and larger thrust forces, respectively. Additionally, the market expansion into areas further offshore, often means that these new larger turbines, as well as their support structures, are exposed to more severe environmental conditions (wind and waves) and are designed for higher cut-out wind speeds, i.e., 30 m/s (Vestas, 2021). In Europe, for example, the expansion into the northern North Sea faces the challenge of not only more frequent storms but also younger sea states, with a wider wave energy density spectrum that stretches into higher frequencies (Holthuijsen, 2007). The above, in combination with higher towers and heavier RNAs, means that, in order to maintain support structure natural frequencies adequately far from wave spectra peak frequencies, the industry might have to orient towards stiffer, sturdier structures.

Another important challenge for the offshore wind industry, is the increase of water depth in potential areas of interest, both in Europe and Worldwide. This, in combination with the increasing operational and environmental loads mentioned above, results in ever-higher overturning moments and lateral forces acting on the support structures of offshore WTG. Consequently, spatial foundation concepts start to gain momentum as a primary choice, rather than a complementary one. Damiani et al. (2016), for example, compared the steel weight and LCOE of monopile and jacket solutions for 6 different case studies along the Eastern US coast and the Gulf of Mexico. For water depths larger than 40 m, the jacket solution yielded lower steel mass and LCOE. As mentioned, in paragraph 1.2.2, jacket foundations have doubled their share in announced projects, compared to existing ones, and according to (Offshore magazine, 2020), Sif, KCI and Smulders are jointly developing a new product line called ‘The revival of the Tripod’ to compete with the monopile for depths ranging from 40 to 70 meters.

Both the jacket and the tripod can use either conventional pile groups (skirted piles) or suction installed caissons (suction buckets) for their foundation and installation. Pile-driving for jackets and tripods is simpler and less noisy compared to that of a monopile due to the relatively smaller size of the skirt piles. However, the increasingly stricter regulations regarding noise mitigation that the wind industry is facing from state agencies, like the BSH in Germany, the RVO in the Netherlands or the EPA in the United States, make the sound-proof solution of suction buckets more and more popular.

As a result, the selection of the appropriate foundation concept for each project is no longer straightforward and depends on local conditions. For example, Lozano-Minguez et al. (2011) have proposed an analytical method of selection between a monopile, jacket and tripod solution for a 5 MW WTG installed at 40 m water depth. They graded three different designs based on 9 attributes (economic, environmental, structural) and constructed a multi-criteria analysis decision matrix based on the TOPSIS method, comparing each attribute value with the corresponding ideal one. The study showed that the support structure closer to the ideal solution was the tripod (0.61/1.00), followed by the jacket (0.55) and the monopile (0.44).

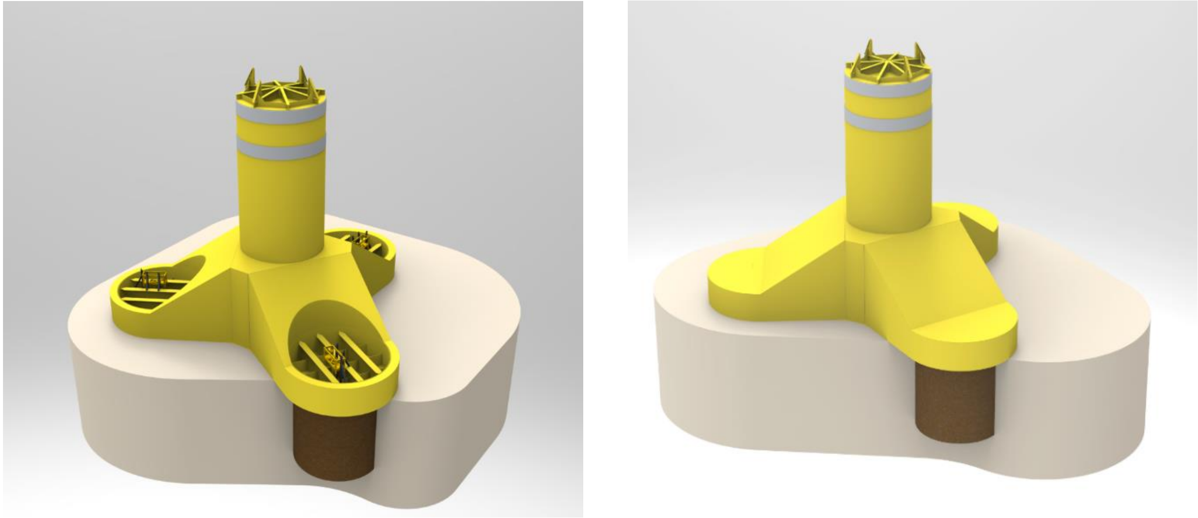

Figure 1-4 TSPC configuration: central column, connection beams and suction piles (SPT Offshore)

1.4 TSPC - Advantages and Challenges

SPT Offshore, a leading offshore contractor for suction pile anchors and foundations, is developing an offshore WTG foundation concept that aims to combine the advantages of a spatial structure, like the tripod, with those of suction installation (SPT Offshore, 2021). The Tri-Suction Pile Caisson (TSPC) consists of a group of three suction piles (caissons), relatively close to each other in a clustered formation, bound rigidly to a central column, reminiscent of the conventional monopile. The acting loads are transferred from the central column, located above the centre of gravity of the foundation, to the pile heads through a set of short shear steel beams (Figure 1-4).

The TSPC can be modularly assembled in a construction yard dry dock and then wet-towed to site, thus, not requiring a heavy lift vessel for the installation (Figure 1-5). The suction piles are installed silently and swiftly, and once in place, the transition piece can be installed with a conventional crane vessel, connected to the foundation with a double slip joint. The reverse sequencing can be used for full-no trace decommissioning.

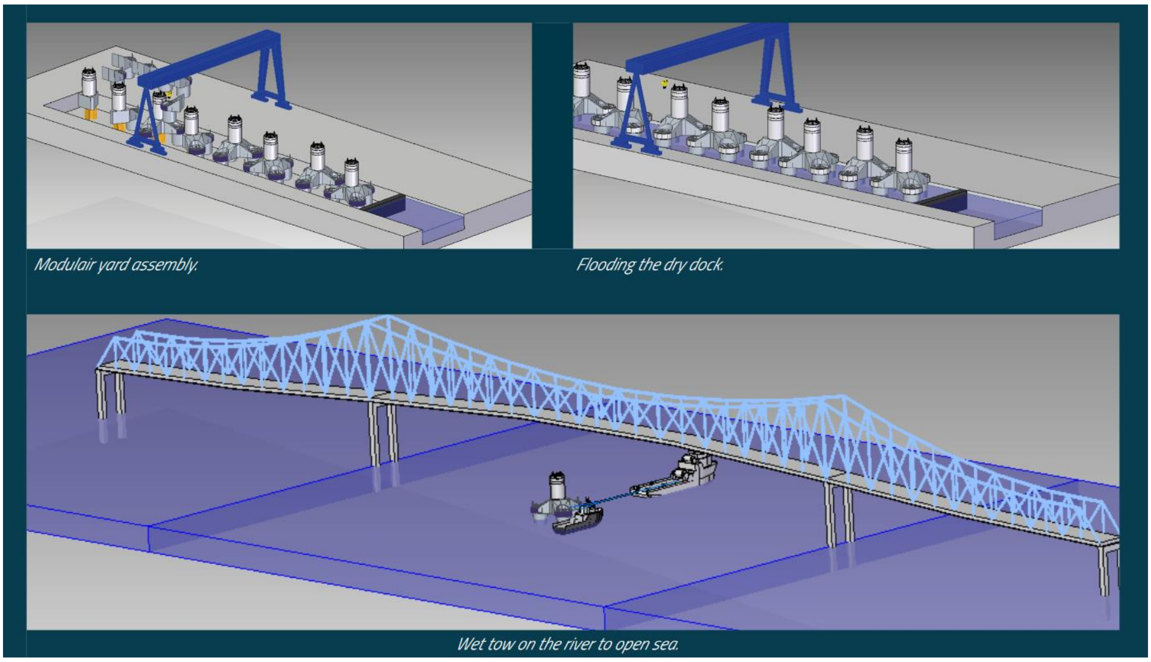

Figure 1-5 TSPC dry dock assembly and wet tow to site (SPT Offshore, 2021).

A big part of the TSPC steel is comparable to cheap “monopile steel” while making use of suction pile foundation performance. The concept is designed to accommodate wind turbines up to 15M W and water depths up to 60 m. Its innovative nature combines proven technologies, like monopile superstructure behaviour and suction foundations, but it also brings new engineering challenges, from a structural, procurement as well as geotechnical viewpoint. This thesis will focus on the latter.

As mentioned in section 1.2.1, the monopile is the offshore wind industry’s favourite and has extensive guidelines, design standards and research available (DNV GL, 2018). Similarly, suction bucket foundations have seen application in offshore projects like wind farms, oil and gas platforms, subsea installations or mooring anchors (Andersen et al., 2005) with existing design standards and research (Sturm, 2017). However, generally applicable design and practice guidelines are not available for the geotechnical design of a clustered suction bucket foundation, like the TSPC. Given the clustered formation of the suction buckets, their interaction, individually and in combination, with the soil around them, must be understood. Furthermore, the developing failure mechanism can also be affected by the stiffness of the connection beams (Choo et al., 2006). Generally, the behaviour of a foundation is expected to differ for cohesive or non-cohesive soils, but this is even more evident for suction installed foundations (Houlsby et al., 2005a). Thus, the main challenge from a geotechnical perspective lies in the identification and quantification of those specific factors, like geometrical configuration, soil type or acting load combination, that influence the behaviour of the TSPC foundation in cohesive and non-cohesive soils.

1.5 Literature Review

Prior to analysing the TSPC soil-structure interaction, a literature review was conducted to assess the state-of-the-art around relevant offshore wind geotechnical applications and, more specifically, suction foundations and spatial foundation concepts.

Suction buckets, piles, or caissons (the distinction being mostly associated with the embedment ratio) are often the preferred foundation type for either jacket structures, tripods or mono-caissons, due to their subtlety and fast and silent installation. (Randolph & Gourvenec, 2011). They exhibit strong coupling between horizontal and vertical stiffness and strength due to being an intermediate foundation and their failure mode heavily depends on the load combination and embedment ratio (Karapiperis & Gerolymos, 2014). As a result, the soil-foundation system is typically considered as one entity described by VHM, i.e., vertical, horizontal and moment, envelope diagrams (3D yield surface plots), where the capacity of the system against one load component is affected by the load level of the other two. In sands, it is common for the yield surface to be normalised by the V component reducing it to a 2D diagram (Villalobos et al., 2009). Although VHM envelopes are available from different sources for individual suction buckets, relations for clustered pile formations, like the TSPC, are not available in literature or design guidelines.

A very common topic discussed in offshore geotechnics is drained and undrained soil response. Lambae and Whitman (1979) describe that the water in the pores of saturated soils tends to resist volumetric changes imposed on the soil skeleton by shearing or compressive loads. As a result, excess pore pressures develop if the pore water is not allowed to drain fast enough, which in turn is affected by the combination of loading rate and soil permeability. Clayey (cohesive) soils have low permeability, whereas sandy (cohesionless) soils have high permeability and for typical offshore engineering applications, exhibit undrained and drained (in principle) behaviour, respectively.

During shearing, loose soils tend to contract and dense soils tend to dilate until the soil mass reaches a void ratio (indicative of volume) at which no further volumetric change occurs, defined as the critical state (Randolph & Gourvenec, 2011). In undrained conditions, contractive loose and dilative dense soils develop excess positive and negative (suction) pore water pressures, respectively, that, in turn, affect the load-bearing capacity of the soil skeleton by altering the effective stresses between soil particles.

This distinction is particularly important for suction foundations, like the TSPC, since it affects their installation process as well as their in-place behaviour (failure mechanism, stiffness). Positive pore pressures reduce effective stresses, thus, reducing soil shear resistance, while suction increases effective stresses and shear resistance (Randolph & Gourvenec, 2011). A characteristic example of undrained behaviour is the reverse end-bearing capacity of suction foundations under tension that, if considered during design, heavily increases their pull-out capacity.

Houlsby and Byrne (2005a, 2005b) describe the installation procedure in sand and clay. In both cases, the initial penetration of the seabed is achieved with the self-weight of the foundation with the next step being the application of suction on the inside of the caissons via a hydraulic pump on the top plate that creates a pressure differential between the outside and inside. In sand, an inward flow of water along the shaft of the caisson is achieved that decreases the effective weight of the soil inside the caisson but, most importantly, reduces the soil resistance at the tip. The limitation of this method is the potential of water flow reaching a critical hydraulic gradient that corresponds to zero inner soil plug effective weight and, thus, liquefaction. Theoretically, the above allows for maximum embedment ratios of 1, however, industrial experience indicates that this is a conservative value. In clay, due to its undrained response, suction pressure is achieved beneath the top plate of the caisson that provides an additional vertical load to achieve desirable penetration. The limitation, in this case, is pump capacity and potential water cavitation in shallow depths due to small values of absolute pressure.

In layered soil profiles, and specifically, in the case of a clay layer above a sand deposit, certain mitigation measures need to be taken. Seepage flow is blocked by the impermeable clayey layer and the necessary sand resistance reduction is not possible. To avoid that, a friction breaker is used to create a gap along the caisson skirts to allow seepage through clay (Sturm, 2017). Once desirable penetration is achieved, the top plate seal is closed and grout is used to avoid differential settlements and pumping effects on the caisson shafts and, additionally, provide structural support to the top plate against large deflections and fatigue. Alternatively, structural steel, hard rubber or composite components can be used for the same purpose, if grouting offshore work is deemed not cost-effective (Sturm, 2017).

Houlsby et al. (2005a) provide an overview of existing lab and field tests for monopod and tetrapod suction foundations. They compare results from different studies by normalizing loads using the caisson radius plus the soil specific weight for sands and undrained shear strength for clays. For sand, despite not matching perfectly quantitatively, lab and field tests showed similar results. Under symmetric cyclic load, monopods stiffness would gradually reduce with a consequent increase of hysteresis. Similar hysteretic behaviour with reduction of secant stiffness was also observed in monopod tests in clay. In the case of tetrapods lab tests in clay, the limited data indicated a sensitivity of tensile capacity to prior compressive loading. For tetrapods in sand, a stiff response was observed for cyclic vertical loading under small amplitude and within the compressive regime. But when the amplitude increased and tensile values were reached, that was followed by immediate soil relaxation, hysteretic loops and strain accumulation. Similar results were reported by Houlsby et al. (2005c, 2006) were in field tests of monopods, high sensitivity to tensile cyclic loading was observed in sand with consequent soil relaxation and foundation settlement.

The above research is used as a reference in multiple pieces of literature regarding suction caissons, as well as design guidelines (Cathie et al., 2019) that cover multiple aspects like the LRFD design approach, seabed preparation, geophysical survey and in-situ testing, hazards, and mitigation measures.

Research that specifically covers the application of suction buckets in tripod foundations is rather limited, but Choo et al. (2006) have conducted centrifuge model testing in sand comparing the performance of a clustered tripod that of an equivalent monopod foundation of equal area. The centre-to-centre distance in the clustered formation was equal to 1.5 times the diameter of the caissons that had an embedment ratio of 1.2. Both foundations were subjected to a combination of lateral force and overturning moment. The tripod initially exhibited a response similar to that of the monopod, however, after structural yielding of the connection beam, the pile in tension shifted from translational-rotational behaviour to pure uplift. The above indicated that in order to guarantee a more global, and potentially beneficial, response of the foundation, a rigid connection is required. Kim et al. (2009) used a similar configuration for numerical comparison of a tripod and a monopod in sand. They observed that, compared to the monopod, the tripod foundation was more efficient against rotational loading and the critical direction was the one corresponding to a single pile in tension.

1.6 Research Objective

The TSPC is a concept that aims to bridge the gap between shallow and deep-water depths for offshore wind farm applications. To fully harness its strategic and innovative advantages, like the modularity and easy transportation/installation, it needs to become economically competitive with already proven technologies, like the monopile and the jacket, that are supported by extensive design guidelines and research. From a geotechnical viewpoint, the identification and exploitation of the governing soil-structure interaction mechanisms that act on the TSPC are very limited. As a result, the factors involved with structural steel and manufacturing complexity reduction, are not yet quantifiable. The objective of this thesis is:

To improve the understanding of the soil-structure interaction in the TSPC foundation

This results in the overall research question:

How does the TSPC foundation interact with cohesive and non-cohesive soils?

Given that the TSPC concept was developed based on the experience of SPT Offshore with suction bucket applications, the following research sub-questions can be formulated:

1. What are the essential similarities and differences between the TSPC and the SBJ with respect to soil-structure interaction?
2. Which failure mechanisms are dominant for static loading of the TSPC in sand and clay?
3. How does the centre-to-centre distance of the suction buckets affect these failure mechanisms?
4. How does the lateral and rotational stiffness of the foundation evolve for different load levels of the governing load combinations?

1.7 Aberdeen Offshore Wind Farm

AOWF (Aberdeen Offshore Wind Farm) is located approximately 2.4km off the coastline of Aberdeenshire at Blackdog, on the North-East coast of Scotland. Specific mention of bathymetry and metocean conditions will be made in chapter 2.

As described above, real-scale or lab testing for tripod suction foundations, like the TSPC concept, is limited. For that reason, it was deemed legitimate to use data from an existing project, as a case study, for the sake of comparison of the TSPC configuration with an in-place SBJ foundation. Additionally, thanks to the involvement of SPT Offshore as the contractor responsible for the geotechnical design of the AOWF project, the writer was able to secure high quality and extensive soil lab and in-situ data for the calibration of the soil parameters in consequent analyses. Moreover, in the project basis of design document, sufficient metocean data were provided for the calculation of the acting environmental loads. Finally, the values of the maximum moment and lateral force used in the AOWF design, as well as the sizing of the SBJ footings, can serve as partial validation of subsequent results in this work.

1.8 Tool Selection

The environmental load calculations, natural frequency analysis and geotechnical analyses have been carried out using both analytical and finite element analyses.

- Microsoft Excel (Microsoft 365 MSO) was used for most of the environmental load calculations; finite element analyses post-processing and book-keeping.
- MATLAB R2017a – Academic version was used for the calculation of the acting thrust force on the RNA during turbine operation
- PLAXIS 3D AE was used for the FEM of the TSPC foundation and the soil-structure interaction analyses conducted in this work.

Regarding the selection of numerical modelling software, certain commercial and academic options were initially considered. ABAQUS is a popular finite element modelling (FEM) software that is used for a variety of applications, but since it is not specifically targeted for geotechnical applications, it lacks an extensive library of soil constitutive models. FLAC is a finite difference modelling (FDM) software suitable for advanced geotechnical analyses and dynamic simulations that is, however, not particularly user friendly. OpenSees is an academic FEM software developed at Berkeley University that despite offering an extensive geotechnical library, it lacks a graphical user interface, making it unfriendly to the user. Finally, PLAXIS 3D is a commercial FEM software directed at geotechnical applications. It offers a wide range of soil constitutive models, it is straightforward to use, and both SPT Offshore and the writer have experience with its applications, making it the obvious choice.

1.9 Thesis Outline

Figure 1-6 provides a visual representation of the procedure followed in this work, as well as the synapses between individual processes.

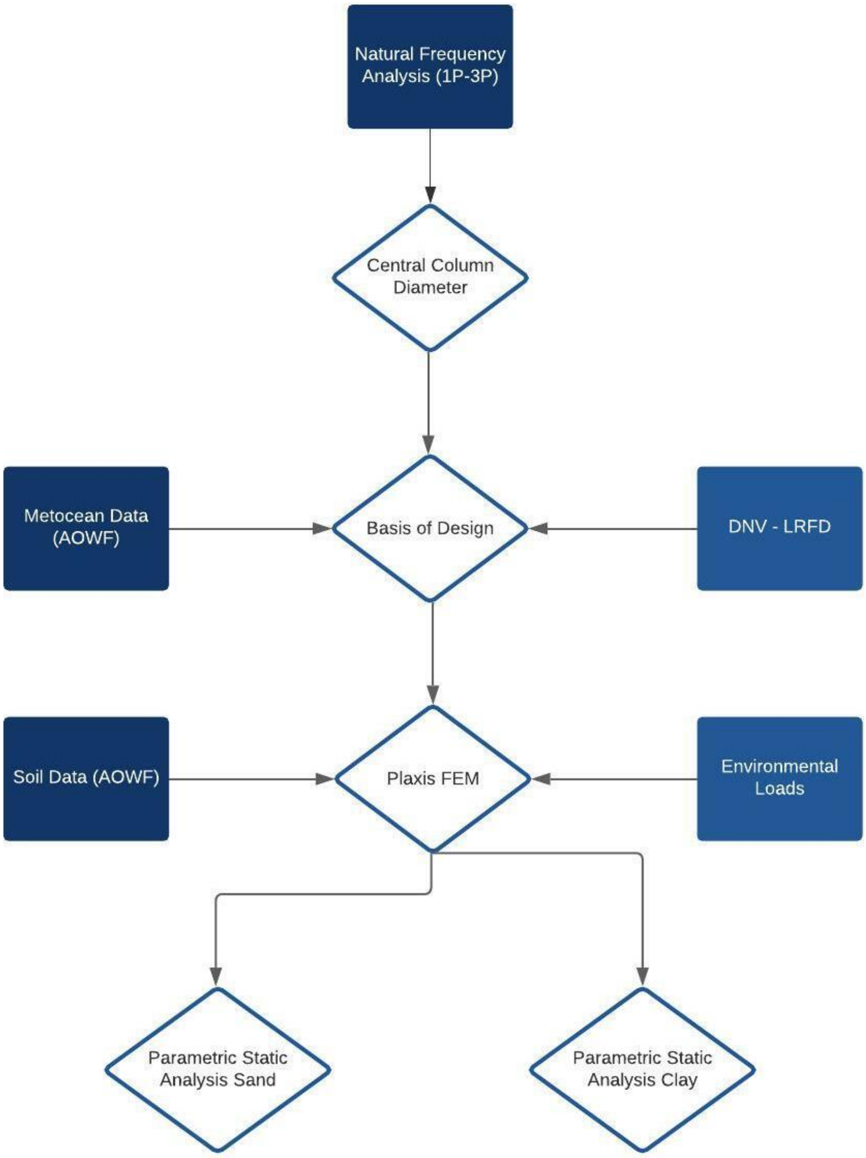

Figure 1-6 Thesis outline representation

2 Basis of Design

This chapter will include an overview of the relevant data available in the AOWF documents provided to the writer by SPT Offshore, as well as the basic design assumptions made regarding the TSPC and the superstructure. The above will be used for a preliminary natural frequency analysis (NFA) to ensure that the fundamental frequency of the integral structure is outside of the WTG 1P-3P range and not overlapping with peak wave frequencies. The results of the NFA, along with the ultimate limit state (ULS) load combinations, will be used as input in the calculation of the environmental loads in the following chapter.

2.1 Natural Frequency Analysis

The purpose of the natural frequency analysis (NFA) is to determine the diameter of the TSPC central column. The procedure is similar to the monopile case with the difference being in the fixed length of the central column, assuming a preliminary centre of rotation on the mudline level due to the stiffer TSPC tripod foundation, compared to the monopile, where the centre of rotation is typically 1-2 times the diameter below the seabed. Initially, the design elevations need to be determined, based on local metocean conditions and wind turbine characteristics.

2.1.1 Water Level

According to the “Bucket Foundation Design Basis” document (SPT Offshore, 2017a), the water depth in AOWF varies from 19.86 m LAT to 31.54 m LAT. However, for this study, only the larger water depth, i.e., 31.54 m LAT will be used as it generates higher hydrodynamic loads and simplifies wave load calculations by allowing linear wave theory approximation for intermediate water depth (Holthuijsen, 2007). For simplicity, an approximative MSL of 34 m will be adopted with a maximum tidal range of ±2.32 m as summarized below:

Table 2-1: Tidal ranges relative to MSL

Water Depth	34	[m]
Lowest Astronomical Tide	-2.32	[m]
Mean Sea Level	0	[m]
Highest Astronomical Tide	2.32	[m]

2.1.2 Wind Turbine Generator

The WTG model in AOWF is the Vestas V164 8.0 (8.4MW). The specifications are listed below as mentioned in (SPT Offshore, 2017a; Vestas, 2011; EOWDC, 2021; Desmond et al., 2016).

Table 2-2: Vestas V164 8.0 Specifications for AOWF.

Rotor Diameter	164	[m]
Hub Height	120	[m]
Cut-in Speed	4	[m/s]
Rated wind Speed	12.5	[m/s]
Cut-out Speed	25	[m/s]
Rotor Range	4.8-12.1	[rpm]
RNA Weight	480	[t]

2.1.3 Marine Growth

The increase of the central column diameter due to marine growth was not considered in the subsequent natural frequency analysis because of the lack of site-specific data. The effect of marine growth was incorporated, however, in the hydrodynamic drag coefficient used in the environmental load calculations of chapter 3, as per (DNV GL, 2016).

2.1.4 Design Elevations

As mentioned above, the starting point of the NFA was the selection of appropriate design elevations for the superstructure (central column, transition piece and tower), which are summarized in Table 2-3.

Table 2-3: Superstructure design elevations relative to MSL.

Mudline	**d**	**-34**	**[m]**
Splash Zone	z_{splash}	-5	[m]
High Astronomical Tide	Δz_{HAT}	+2.3	[m]
Storm Surge	Δz_{ss}	2.65	[m]
Wave elevation	ζ	9.9	[m]
Air gap	Δz_{air}	7	[m]
Interface level	**z_i**	**+24**	**[m]**
Blade tip low	$z_{bt,min}$	+38	[m]
Rotor diameter	D_R	164	[m]
Blade tip height	$z_{bt,max}$	+202	[m]
Hub height	**z_h**	**+120**	**[m]**

2.1.4.1 Splash Zone

The lower limit of the splash zone was calculated as per (DNV, 2016) and coincides with the lower part of the transition piece so that no corrosion protection will be necessary for the central column.

2.1.4.2 Storm Surge

The design storm surge for the AOWF location is not included in the available metocean data. In the absence of specific data, the recorded storm surge of 2.65 m during the 5/12/2013 event as monitored by the Aberdeen sea-level monitoring station (IOC, 2021) was used in the design. For reference, this value is within the range of severe storm surge reports (2.5-3.5 m) of the German Federal Maritime and Hydrographic Agency (BSH, 2021). The higher storm surge values monitored in the German North Sea are likely connected to the unfavourable directionality of the most severe storms and coast shape, compared to Aberdeen.

2.1.4.3 Wave Elevation

The maximum wave crest and wave run-up were calculated according to (De Vos et al., 2007) using the 50-year extreme wave height and associated period as well as the highest astronomic tide (HAT) water depth as in Equations 2.1-2.3.

$$\eta_{max} = \frac{H_{max,50}}{2} + k\frac{H_{max,50}}{2}\frac{H_{max,50}}{8}\frac{cosh(kd)}{sinh^3(kd)}\big(2 + cosh(2kd)\big) \tag{2.1}$$

$$u_{top} = \frac{H}{2}\frac{gk}{\omega}\frac{cosh\big(k(\eta_{max} + d)\big)}{cosh(kd)} + \frac{3}{4}k\frac{H^2}{4}\omega\frac{cosh\big(2k(\eta_{max} + d)\big)}{sinh^4(kd)} \tag{2.2}$$

$$R_{u2\%} = \eta_{max} + 2.71\frac{{u_{top}}^2}{2g} \tag{2.3}$$

Where:

η_{max}	maximum wave crest elevation	d	water depth
$H_{max,50}$	50-year maximum wave height	u_{top}	horizontal particle velocity at wave crest
k	wavenumber	$R_{u2\%}$	2% excess run-up height

2.1.4.4 Interface Level

The interface level, coinciding with the bottom part of the tower and upper part of the transition piece, was calculated and rounded up to an integer by summing the listed design elevations of Table 2-3 with 2 meters of contingency.

2.1.4.5 Blade clearance and Hub Height

The resulting blade clearance for an interface level of 24m and a hub height of 120m is 14m, which can be considered non-optimal in terms of structural steel. However, considering potential environmental reasons (bird flight altitude) and for the sake of consistency with the AOWF case study, the hub height of 120m was used.

2.1.5 Structural Dimensions

Using the design elevations as input, the diameters and thicknesses of the tower, transition piece and TSPC central column were defined to satisfy the 1st eigenfrequency, i.e., “soft-stiff” design criterion. Specifically, the 1st natural frequency of the integral structure, including the foundation, should be within the 1P-3P range, i.e., the upper part of the rotor frequency range and lower part of the blade crossing frequency range. The structural dimensions used in the NFA are summarized below:

Table 2-4: Superstructure diameters and thicknesses.

Tower top diameter	$D_{t,top}$	4.5	[m]
Tower top thickness	$t_{t,top}$	30	[mm]
Tower bot diameter	$D_{t,bot}$	6.5	[m]
Tower bot thickness	$t_{t,bot}$	40	[mm]
TP top diameter	$D_{TP,top}$	6.5	[m]
Tp top thickness	$t_{TP,top}$	65	[mm]
Tp bottom diameter	$D_{TP,bot}$	7.5	[m]
Tp bottom thickness	$t_{TP,bot}$	75	[mm]
Central column diameter	D_{cc}	7	[m]
Central column thickness	t_{cc}	70	[mm]

The fundamental frequency was calculated with the TU Delft MS Excel tool “*NF stepped monotower*”. It uses the Rayleigh method to provide an upper boundary approximation of the 1st natural frequency for a distributed mass cantilever beam with varying dimensions (Temple, 1952). The choice of structural dimensions was made based on industrial standards with a *D/t* ratio equal to 160 and 100, for the tower and central column, respectively. In conventional monopiles the *D/t* ratio usually take values between 70-80, however, in this case, the central column will not be subject to hammering since the TSPC does not require pile driving (Wandji et al., 2015). Thus, in the absence of intense axial loads, a smaller thickness was viable. For this preliminary NFA, the centre of rotation for the TSPC foundation was assumed at the mudline (as opposed to approximately one diameter below mudline for conventional monopiles), resulting in the 1st natural frequency of Table 2-5.

Table 2-5: Preliminary 1st natural frequency for the integral structure.

Vestas V164 8.0	1P max	0.202	[Hz]
TSPC	**1st NF**	**0.233**	[Hz]
Vestas V164 8.0	3P min	0.240	[Hz]

2.2 Metocean Data

The metocean data for the AOWF area retrieved from the SPT basis of design (SPT Offshore, 2017a) include significant wave height and period information but do not include wind climate data, or wind-wave correlation charts. Instead, relevant design load combinations, sea-states and wind velocities were available in the "Design Checks for 8-8MW OPTI TIP Mode" document (Ramboll, 2018) that correspond to rated (12.5m/s), cut-out (25m/s) and 50-year return period (44m/s) wind velocity, respectively. They are summarised below:

Table 2-6: Design significant wave height, peak wave period, wind and current velocity.

	H_s [m]	T_p [s]	v_{wind} [m/s]	$v_{current}$ [m/s]
Rated wind speed	2.2	6.6	12.5	1.01
Cut-out wind speed	6.0	11.2	25	1.14
50-year storm	7.8	12.3	44	1.22

2.3 Ultimate Limit State (ULS)

2.3.1 Load Factors

In-place loads generated from the available metocean data were combined using the LRFD approach and contained load factors in accordance with DNV design standards (DNV GL, 2016). Load factors as presented in Table 2-7 were used:

Table 2-7: Load Factors

Environmental Loads	**Permanent Loads**	
	Favourable	Unfavourable
1.35	0.9	1.1

2.3.2 Material Factors

For suction bucket foundations the following partial soil resistance material factors were used in safety analyses according to (DNV GL, 2018).

Table 2-8: Soil resistance material factors for the in-place condition.

Design Phase	**Component**	γ_m
In-place	Effective Stress Analysis	1.15
	Total Stress Analysis	1.25

2.3.3 Load Combinations

As mentioned in paragraph 2.2, the metocean data retrieved from (Ramboll, 2018) include, among other, 3 characteristic load combinations that sufficiently cover the spectrum of environmental loads acting on the foundation for the purpose of this thesis. Specifically, DLC 3.2 assumes production at rated wind speed, thus, maximum rotor thrust force and emphasizes the effect of overturning moment acting on the foundation. Similarly, DLC 6.1 assumes parked turbine and severe sea state, emphasizing the effect of large lateral loads instead. Below is a summary of the load cases as per (DNV GL, 2016) that will be used in the subsequent calculations in chapter 3.

Table 2-9 ULS load combinations.

Limit State	Load Combination	DLC	Wind	Waves	Current
ULS	**1**	**3.2**	Rated	Hs = E[Hs|Vhub]	1-year
ULS	**2**	**2.3**	Cut-out	Hs = E[Hs|Vhub]	5-year
ULS	**3**	**6.1**	50-year	50-year	50-year

3 Environmental Loads

The environmental loads include hydrodynamic (waves and current) and aerodynamic (thrust force and wind shear) loading. The input for the calculation of these loads were the structural dimensions in Table 2-4, the metocean data in Table 2-6 and the load combinations in Table 2-9.

3.1 Hydrodynamic Load

The hydrodynamic load consists of a drag and an inertial component. The drag component is related to water particle velocity and is a superposition of wave and current induced drag forces normal to the structure. The inertial component is related to water particles acceleration, thus, is only affected by waves, assuming constant current velocity.

3.1.1 Current

For each load combination, the current velocity was split into a tidal and a wind-induced component. The tidal component was taken with the spring tide value corresponding to Aberdeen and equal to 0.6m/s (OESEA3, 2016), with the remaining value in each case being the wind-induced current. According to (DNV GL, 2016), the current velocity depth profile follows a power law for the tidal component (Equation 3.1) and is linear for the wind component (Equation 3.2).

$$U_{tide}(z) = U_{tide0}\left(\frac{d+z}{d}\right)^{\frac{1}{7}} \tag{3.1}$$

$$U_{wind}(z) = U_{wind0}\left(\frac{d_0+z}{d_0}\right) \tag{3.2}$$

Where:

z	vertical coordinate from still water level, positive upwards
U_{tide0}	tidal current at still water level
U_{wind0}	wind-induced current at still water level
d	water depth from still water level (taken as positive)
d_0	reference depth for wind-generated current; d_0 = 50 m.

3.1.2 Waves

A sea state is characterized by a significant wave height and peak period. However, in the hydrodynamic load calculations, the maximum wave height and the associated period were used. The mean zero-crossing period of the sea states corresponding to the load combinations mentioned in section 2.2 was calculated from the peak period using Equations 3.3 and 3.4 and, consecutively, the number of waves for a 3-hour storm duration (Equation 3.5), according to (DNV GL, 2016).

$$T_z = T_p\sqrt{\frac{5+\gamma}{11+\gamma}} \tag{3.3}$$

$$\gamma = \begin{cases} 5 & for\ \frac{T_p}{\sqrt{H_s}} \leq 3.6 \\ e^{\left(5.75-1.15\frac{T_p}{\sqrt{H_s}} \leq 5\right)} & for\ 3.6 \leq \frac{T_p}{\sqrt{H_s}} \leq 5 \\ 1 & for\ 5 \leq \frac{T_p}{\sqrt{H_s}} \end{cases} \tag{3.4}$$

$$N = \frac{T_S}{T_z} \qquad \text{where } T_S \text{ is the sea state duration, equal to 3 hours} \tag{3.5}$$

Next, the maximum wave height and the associated period were calculated through Equations 3.6 and 3.7:

$$H_{max,mean} = \left(\sqrt{\frac{1}{2} lnN} + \frac{0.2886}{\sqrt{2 \ln N}} \right) H_s \tag{3.6}$$

$$11.3\sqrt{H_S(V_{hub})/g} \leq T \leq 14.3\sqrt{H_S(V_{hub})/g} \tag{3.7}$$

The wave frequency and design water elevation were used as input in the dispersion relationship (Equation 3.8) for the calculation of the wavenumber, k, using the Eckart approximation of Equation 3.9 for intermediate water depth (Holthuijsen, 2007).

$$\omega^2 = gk \tanh(kd) \tag{3.8}$$

$$\begin{gathered} kd \approx \alpha(tanh\alpha)^{-1/2} \\ \alpha = \omega^2 d/g \end{gathered} \tag{3.9}$$

Finally, the horizontal particle wave-induced velocity and acceleration amplitudes were calculated using Equation 3.10 according to linear (Airy) wave theory (Holthuijsen, 2007).

$$u_x = \omega\eta \frac{cosh[k(d+z)]}{\sinh(kd)} sin(\omega t - kx) \tag{3.10}$$

Linear wave theory, however, only provides kinematic values below and up to still water level. To incorporate the wave crest velocities, the Wheeler stretching extrapolation method was used (Mohd & Noor, 2013).

3.1.3 Morison’s Equation

Morison’s equation (Equations 3.11-3.15) is used in the offshore industry to calculate the hydrodynamic force acting on cylindrical structures, consisting of an inertial and a drag component, associated with water particle acceleration and velocity, respectively, thus being 90 degrees out of phase (DNV GL, 2016). As mentioned in section 2.1.3, marine growth will be considered using an appropriate surface roughness coefficient, k, in Equation 3.13.

$$F = F_M + F_D = \int_{-d}^{\eta(t)} C_M \rho\pi \frac{D^2}{4} \ddot{x} dz + \int_{-d}^{\eta(t)} C_D \rho \frac{D}{2} |\dot{x}| \dot{x} dz \tag{3.11}$$

Where:

C_M	inertia coefficient	$\dot{x}$	horizontal water particle velocity
C_D	drag coefficient	$\ddot{x}$	horizontal wave-induced acceleration of water
D	diameter of the cylinder	z	water depth from still water level (negative)
ρ	density of water	$\eta(t)$	wave crest

$$C_M = max\{2.0 - 0.044(KC - 3); 1.6 - (C_{DS} - 0.65)\} \tag{3.12}$$

$$C_{DS} = \begin{cases} 0.65 & for\ k/D < 10^{-4} \text{ (smooth)} \\ \dfrac{29 + 4log_{10}(k/D)}{20} & for\ 10^{-4} < k/D < 10^{-2} \\ 1 & for\ k/D > 10^{-2} \text{ (rough)} \end{cases} \tag{3.13}$$

$$C_D = C_{DS} * \psi(C_{DS}, KC) \tag{3.14}$$

$$KC = u_{max}\,T/D \tag{3.15}$$

Where:

KC	Keulegan-Carpenter number
C_{DS}	drag coefficient for steady-state flow
k	surface roughness, taken as 0.05 m to account for marine growth
u_{max}	maximum horizontal particle velocity at still water level
T	wave period

The solution of Morison's equation is time-dependent, and the maximum force is not a straightforward combination of the amplitudes of the drag and inertial components. For this study, a slightly conservative approximation was made for the maximum total force by square root superposition (Equation 3.16), considering that the two components are 90 degrees out of phase.

$$F_{max} = \sqrt{F_{M,max}^2 + F_{D,max}^2} \tag{3.16}$$

3.2 Aerodynamic Load

The aerodynamic load consists of the wind shear acting on the tower as well as the thrust force acting on the WTG rotor during operation or the drag force acting on the nacelle during parked or idle conditions.

3.2.1 Wind Shear

A logarithmic profile was assumed for the wind speed profile (Equation 3.17) according to (IEC, 2005). The aerodynamic drag force acting on the tower was calculated as in Equation 3.18.

$$u(z) = u(z_r)\frac{\ln(z/z_0)}{\ln\,(z_r/z_0)} \tag{3.17}$$

$$F_{D,aero} = \int_{-d}^{\eta(t)} C_D\,\rho\frac{D}{2}u^2 dz \tag{3.18}$$

3.2.2 Thrust Force and Nacelle Drag

During operation, the thrust force acting on the WTG rotor was calculated using the "*TURCAL*" MATLAB tool by TU Delft, which provides a quick approximation based on the Blade Element Momentum theory:

$$P = C_p \frac{\rho}{2} A u_{hub}^3 \tag{3.19}$$

Where:

C_D	aerodynamic drag coefficient	z_0	roughness length, taken as 0.0002m for the North Sea
ρ	density of air		
$u(z)$	normal wind velocity	C_p	power coefficient
z	height above sea level	u_{hub}	wind velocity at hub height
z_r	reference height above sea level		

The blade properties used in the tool are scaled from the DOWEC 6MW turbine, so an additional calibration is necessary after the initial calculation. In parked conditions, the aerodynamic drag force on the RNA was calculated using the corresponding hub height wind velocity and drag coefficient equal to 1.16 (Mohammed et al., 2016), assuming a rectangular cross-section for the V164-8 nacelle with dimensions 8m x 8m (Vries, 2013).

3.3 ULS Load Combinations

The 3 load combinations presented in chapter 2 were used to calculate the acting loads on the TSPC foundation. The DLC 6.1 case in (Ramboll, 2018) lists values of extreme 50-year wave height and associated period, as well as extreme 50-year wind speed, which will be used directly in load calculations. The DLC 2.3 and DLC 3.2 cases, referring to rated and cut-out wind speed, respectively, mention only significant wave height and peak period values, so the corresponding extreme wave heights and associated periods are calculated as in section 3.1.2. The design values of the environmental conditions are summarized below.

Table 3-1: Load combinations and design environmental conditions.

Limit State	**Load Combination**	**DLC**	**Wind**	**Waves**		**Current**
			u_w [m/s]	**H_{max} [m]**	**T_{max} [s]**	**u_c [m/s]**
ULS	1	3.2	12.5	4.7	9.2	0.89
ULS	2	2.3	25	11.8	15.0	0.95
ULS	3	6.1	44	14.5	16.5	1.22

The resulting environmental loads, factored according to section 2.3.1 acting on the mudline are presented below:

Table 3-2: ULS environmental loads summary.

Limit State	**Load Combination**	**DLC**	**H**	**Hydro**	**Aero**	**M**	**Hydro**	**Aero**
			[MN]	**[%]**	**[%]**	**[MNm]**	**[%]**	**[%]**
ULS	**1**	**3.2**	**4.4**	65	35	**307.1**	24	76
ULS	**2**	**2.3**	**7.0**	85	15	**270.9**	49	51
ULS	**3**	**6.1**	**8.9**	89	11	**275.4**	69	31

For verification purposes, these values are compared to the maximum occurring factored H and M loads as mentioned in the checks against global failure in the Detailed Geotechnical Design of SPT Offshore for the SBJ in the AOWF for the Cluster 4 (B04) case (SPT Offshore, 2017b).

Table 3-3: Comparison of maximum horizontal force and overturning moment for the TSPC and SBJ.

	Max H [MN]	**Max M [MNm]**
TSPC	8.9	307.1
SBJ	10	364

3.3.1 Remarks

It can be observed that the maximum calculated environmental loads for the TSPC are comparable to those of the detailed SBJ design. Although the values were independently calculated for this study, the aerodynamic component of the loading should, theoretically, be the same in both cases since they refer to the same WTG, hub height and wind climate. However, it is not straightforward whether one should expect lower or higher hydrodynamic loads for the TSPC compared to an SBJ for the same wave - current climate and water depth.

The hydrodynamic loads on the TSPC, due to the large diameter central column, are expected to be higher (in comparison to the SBJ) when the inertial part of Morison’s equation (3.11) is dominant, i.e., for smaller wave periods. On the other hand, the loads acting on the SBJ are affected by the slender members of the jacket meaning that they are drag dominated, thus, being larger (in comparison to the TSPC) for longer wave periods. As a result, in larger wave conditions, e.g., the DLC 6.1 design storm, the SBJ should experience relatively larger wave loads compared to the TSPC, which could mean higher maximum lateral force, while for smaller waves during operation, the situation is reversed and the TSPC is expected to experience higher wave loads.

Conclusively, the calculated design load values fall within reasonable boundaries and are appropriate for subsequent analyses.

4 Soil Model Calibration

As described in previous chapters, AOWF was chosen as a case study due to the wide range of available data. SPT Offshore provided the writer with extensive geotechnical site investigation data (Fugro, 2016), which will be used to calibrate constitutive soil parameters in the FEM analyses of the following chapters.

4.1 Soil Unit Overview

The survey conducted by Fugro (2016) was naturally focused on the locations of the 11 WTG in the AOWF, identifying 4 major soil units: Ia, Ib, II and III, corresponding to loose-very dense sand, very loose-medium dense sand, soft to very stiff clay and firm to very stiff clay, respectively. A summary of these units can be found in Table A-1 of Appendix A.

Due to variations between the different locations, SPT Offshore in the design basis document (SPT Offshore, 2017a), have discretized soil formations into 3 major cases with similar soil units and layer depth distribution that are summarized in Table A-2 of Appendix A. Each of these cases is represented in most of the following laboratory tests by one WTG location, i.e., locations A02, B02 and B06.

Since the purpose of this thesis is not to directly simulate in-situ conditions for AOWF but to use the extensive soil testing available, only two soil units will be used in the analyses of the following chapters in separate uniform profile cases. A uniform profile of soil unit Ib will be used in analyses with sand, and a uniform profile of unit II will be used in analyses with clay.

4.2 Lab Test Overview

As mentioned above, most laboratory tests were conducted from samples retrieved out of 3 characteristic locations. For this thesis, despite variations in soil formations and water depth, only 2 cases will be considered: uniform sand and uniform clay profiles. Additionally, sand and clay properties will be calibrated from tests of all 3 locations. The relevant lab tests included:

- 11 Unconsolidated Undrained Triaxial Tests
- 11 Anisotropically Consolidated Triaxial Compression Tests
- 8 Anisotropically Consolidated Triaxial Compression Tests with Bender Element
- 4 Anisotropically Consolidated Triaxial Extension Tests
- 5 Anisotropically Consolidated Triaxial Extension Tests with Bender Element
- 4 Consolidated Cyclic Triaxial Tests
- 3 sets of 9 Isotropically Consolidated Drained Triaxial Tests
- 9 Constant Rate of Strain Oedometer Tests
- 11 Incremental Oedometer Tests
- 16 Reconstituted Incremental Oedometer Tests
- 17 Direct Simple Shear Tests
- 15 Cyclic Simple Shear Tests
- 42 Plasticity Index Tests
- 11 Fall Cone Tests

An overview of the sampling locations and test types can be found in Tables B-3 and B-4, respectively, in Appendix B. The relevance of each test type and its role in the calibration process is discussed in section 4.5.

4.3 In-situ Test Overview

Supplementary to laboratory test data, a series of in-situ test data was available in the geotechnical site investigation (Fugro, 2016). For each of the 11 WTG locations the tests conducted were:

- 3 sets of cone penetration tests (CPT)
- 2 sets of seismic cone penetration tests (SCPT)

However, only the tests that coincided with the 3 locations used for laboratory test sampling were used in this work, for consistency in comparison and validation. The resulting cone resistance and shear wave velocity profiles for CPT and SCPT, respectively, are not included in this report. Instead, comparison is made between CPT values in discreet soil depths coinciding with those of laboratory test specimens. Further explanation is provided in section 4.5.

4.4 Constitutive Model Selection

Plaxis 3D offers a wide variety of constitutive soil models, suitable for different applications, depending on the geotechnical focus of interest, available soil data and desirable accuracy versus computational speed ratio. The above factors were taken into account in the selection of appropriate constitutive models for sand and clay to be used in this work.

4.4.1 Mohr-Coulomb model

The Mohr-Coulomb (MC) model, as described in the Plaxis 3D material model manual (Bentley, 2020), is a linear elastic perfectly plastic model, that is very popular among geotechnical engineers for a first approximation of soil behaviour. It uses the basic principle of elastoplasticity that strains are decomposed into an elastic and a plastic part:

$$\underline{\varepsilon} = \underline{\varepsilon}^{e} + \underline{\varepsilon}^{p} \tag{4.1}$$

Hooke’s law is used to relate elastic strains to stresses:

$$\underline{\sigma'} = D^{e}\underline{\varepsilon}^{e} \tag{4.2}$$

Plastic strains are proportional to the derivative of a plastic potential function, g, with respect to stresses:

$$\underline{\varepsilon}^{p} = \lambda \frac{\partial g}{\partial \sigma'} \tag{4.3}$$

The plastic yield condition follows the Mohr-Coulomb failure criterion and for the 2D case is:

$$f = \frac{1}{2}(\sigma'_1 - \sigma'_3) - \frac{1}{2}(\sigma'_1 + \sigma'_3)sin(\varphi) - ccos(\varphi) \leq 0 \tag{4.4}$$

Where φ and c are the soil internal friction angle and cohesion and σ'_1 and σ'_3 are the principal effective stresses in the 2D space.

The model’s simplicity allows for a smaller computational cost, compared to more advanced models, as well as considerably fewer input parameters, that make it ideal for calculations in the initial stages of a project or when extensive geotechnical data are not available.

However, perfect elasticity implies a constant (elastic) stiffness modulus, regardless of stress level or type of loading (Figure 4-1). This is significantly important when the evolution of foundation stiffness due to different load levels (load-displacement curves) is of interest. Additionally, the MC model struggles when more than one type of loading conditions is emphasized in a problem, for example, both triaxial and unloading-reloading conditions.

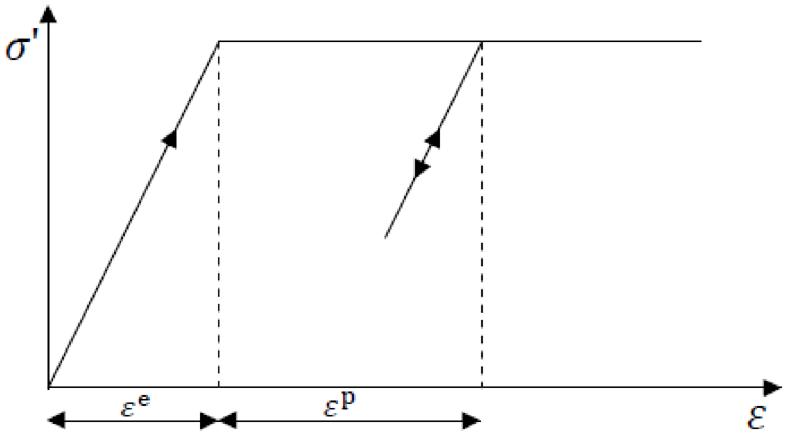

Figure 4-1 Stress-strain relation and failure criterion for the Mohr-Coulomb model (Bentley, 2020).

Finally, when undrained conditions apply, soil strength is represented by the undrained shear strength parameter, S_u, that is equivalent to the cohesion, c. The MC model, however, uses one global S_u value regardless of loading type that cannot accurately describe the soil resistance capacities for different parts of the foundation, e.g., frictional failure on the caisson shafts or triaxial failure beneath the caisson foot.

4.4.2 Hardening Soil model (with small-strain stiffness)

In reality, the strain range in which soils experience only elastic strains, i.e., where they recover from applied straining almost completely after unloading, is very small. The Mohr-Coulomb model assumes that all strains before reaching the failure surface are elastic. On the other hand, the Hardening Soil model (HSM) assumes irreversible (plastic) strains as well as decreasing stiffness due to primary deviatoric (shear) loading (hardening plasticity), (Bentley, 2020). It uses a shear hardening yield function of the form:

$$f = \overline{f} - \gamma^p \tag{4.5}$$

Where $\overline{f}$ is a function of stress and γ^p is a function of plastic strains:

$$\overline{f} = \frac{2}{E_i}\frac{q}{1 - q/q_\alpha} - \frac{2q}{E_{ur}} \tag{4.6}$$

$$\gamma^p = -\left(2\varepsilon_1^p - \varepsilon_v^p\right) \approx -2\varepsilon_1^p \tag{4.7}$$

In which E_i is connected to E_{50}, the secant stiffness controlling plastic straining due to primary deviatoric loading $(\sigma'_1 - \sigma'_3)$ and E_{ur} is the tangent stiffness controlling plastic straining due to primary compression $(\sigma'_1 + \sigma'_3/2)$. Both stiffness parameters are depicted in Figure 4-2.

$$E_i = \frac{2E_{50}}{2 - R_f} \qquad E_{50} = E_{50}^{ref}\left(\frac{c\cos(\varphi) - \sigma'_3\sin(\varphi)}{c\cos(\varphi) - p^{ref}\sin(\varphi)}\right)^m \tag{4.8}$$

$$E_{ur} = E_{ur}^{ref}\left(\frac{c\cos(\varphi) - \sigma'_3\sin(\varphi)}{c\cos(\varphi) - p^{ref}\sin(\varphi)}\right)^m \tag{4.9}$$

Where E_{50}^{ref} and E_{ur}^{ref} are reference stiffness values corresponding to confining pressure, p^{ref}=100 stress units. The quantity q_α (asymptote failure line in Figure 4-2) is connected to failure stress, q_f, as derived from the Mohr-Coulomb failure criterion, with $R_f = 0.9$:

$$q_\alpha = \frac{q_f}{R_f} \qquad q_f = (c\cot(\varphi) - \sigma'_3)\frac{2\sin(\varphi)}{1-\sin(\varphi)} \tag{4.10}$$

Once the failure criterion is met, perfectly plastic yielding occurs as described by the MC model (continuous horizontal branch in Figure 4-2). If the yield condition in Equation 4.5 is met ($f = 0$), then by substitution of Equations 4.6 and 4.7 the plastic component of the vertical strain, ε_1^p, can be found as:

$$\varepsilon_1^p = \frac{1}{E_i}\frac{q}{1-q/q_\alpha} - \frac{q}{E_{ur}} \tag{4.11}$$

For drained triaxial conditions, the elastic vertical strain is given as:

$$-\varepsilon_1^e = \frac{q}{E_{ur}} \tag{4.12}$$

The total vertical strain, being the summation of the above, can be then described as a hyperbolic function of deviatoric stress, q:

$$-\varepsilon_1 = \frac{1}{E_i}\frac{q}{1-q/q_\alpha} \qquad \mathit{for}\ q < q_f \tag{4.13}$$

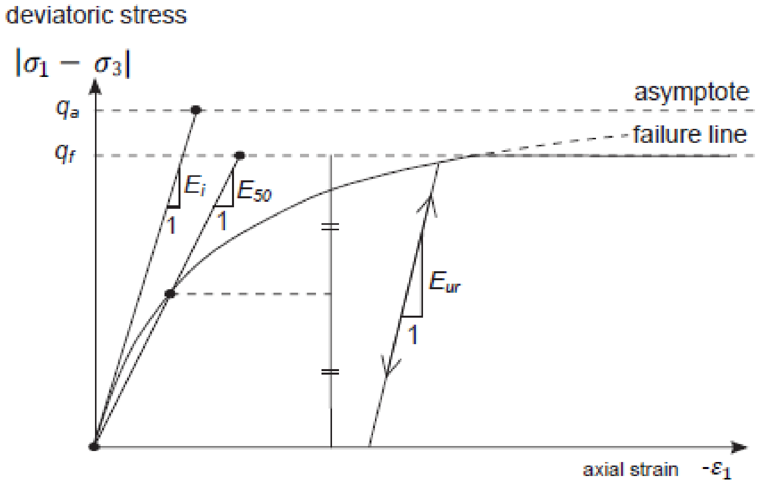

Figure 4-2 Stress-strain relation and failure criterion for the Hardening Soil Model (Bentley, 2020).

The extension of small strain stiffness (HSMsmall), provides an additional sigmoid hyperbolic relation between small strain (elastic) secant shear stiffness, G_s, and shear strain:

$$\frac{G_s}{G_0} = \frac{1}{1 + a\left|\frac{\gamma}{\gamma_{0,7}}\right|} \qquad \mathit{where}\ \ a = 0.385 \tag{4.14}$$

The main advantage of using HSMss over MC is the more realistic gradual transition of soil behaviour from elasticity to plasticity and failure, through intermediate yield surfaces, which provides a more accurate representation of foundation stiffness evolution in drained conditions. In addition, close to failure, in the domain of large strains and non-linearity, HSM behaves the same as MC, being computationally efficient. For these reasons, HSMss was chosen for modelling sandy soil in subsequent FEM calculations.

4.4.3 NGI-ADP model

In undrained conditions, soil load-bearing capacity is described by the undrained shear strength, S_u. In the MC model, one global value of S_u is used. As described above, this forces the user to compromise by selecting a value that approximately describes all stress states. The NGI-ADP model, (Bentley, 2020), gives the option to use anisotropic undrained shear strength with different values for active, passive, and direct simple shear stress paths, S_u^C, S_u^E and S_u^{DSS}, respectively. In addition, a stress path dependent hardening parameter is introduced to account for different failure shear strains:

$$\kappa = 2\frac{\sqrt{\gamma^p/\gamma_f^p}}{1+\gamma^p/\gamma_f^p} \qquad when\ \ \gamma^p < \gamma_f^p;\ else\ \kappa = 1 \tag{4.15}$$

Where γ^p is plastic shear strain and γ_f^p is the plastic shear strain in failure. The yield criterion under 1D triaxial conditions is:

$$f = \left|\tau - (1-\kappa)\tau_0 \cdot \kappa\frac{S_u^C - S_u^E}{2}\right| - \kappa\frac{S_u^C - S_u^E}{2} = 0 \tag{4.16}$$

Where τ is the shear stress and τ_0 is the initial in-situ maximum shear stress. The triaxial compression and extension shear failure stresses and strains can be seen in Figure 4-3(a), while the 3 undrained shear strength limits can be seen at the boundaries of the deviatoric stress plot seen in Figure 4-3(b):

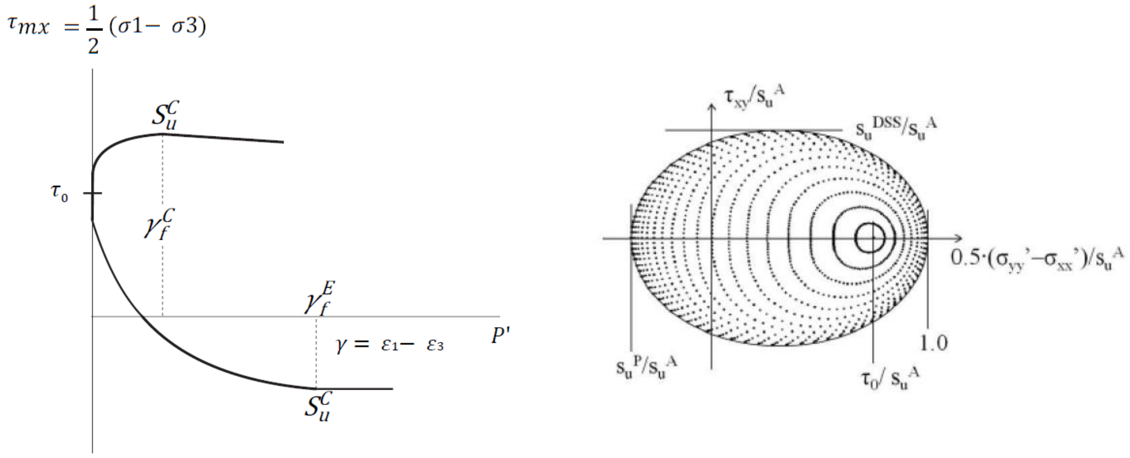

Figure 4-3 (a) Stress-strain curves for triaxial compression and extension. (b) Plane strain deviatoric stress plot with equal shear strain contours. (Bentley, 2020)

The NGI-ADP model is more flexible than the MC model and provides a more spherical description of the stress path evolution and stress-strain relation for undrained analyses without significantly increasing inherent model complexity. Its major drawback is the high number of input parameters that are not always available. However, thanks to the extensive geotechnical data from AOWF, the calibration of NGI-ADP is possible, and it will be used to simulate clayey soil conditions in the analyses.

4.5 Model Parameter Selection

In this section, the laboratory and in-situ test data will be used to calibrate the input model parameters for Plaxis 3D.

4.5.1 Hardening Soil Model (small strain)

HSMss will be used to simulate sand, and specifically soil unit Ib, as mentioned in section 4.1. The model parameters, according to the Plaxis 3D manual, are presented in Table 4-1:

Table 4-1 HSMss input parameters.

γ_{sat}	Specific unit weight	18.9	[kN/m^3]
c	Effective cohesion	0	[kPa]
φ	Effective angle of internal friction	35	[°]
m	Power for the stress-level dependency of stiffness	0.5	[-]
E_{50}^{ref}	Secant stiffness in standard drained triaxial test	33	[MPa]
E_{oed}^{ref}	Tangent stiffness for primary oedometer loading	40	[MPa]
E_{ur}^{ref}	Unloading/reloading stiffness from drained triaxial test	99	[MPa]
ν_{ur}	Poisson's ratio for unloading reloading	0.2	[-]
G_0^{ref}	Reference shear modulus at very small strains	115	[MPa]
$\gamma_{0.7}$	Threshold shear strain at which Gs = 0.722G0	$5 \cdot 10^{-5}$	[-]
R_{inter}	Interface strength coefficient	0.65 / 1.00	[-]

The specific unit weight of saturated sand, γ_{sat}, was retrieved from the SPT Offshore Geotechnical Ground Model and Design Parameters document (SPT Offshore, 2016). The cohesion, c, and angle of internal friction, φ, were averaged from the 3 out of 9 isotropically consolidated drained triaxial tests mentioned in section 4.2, that used samples from soil depths that corresponded to soil unit Ib, while Plaxis guidelines suggest that power coefficient, m, should be taken as 0.5 for sand.

The reference secant stiffness modulus was derived graphically, using scatter data of E_{50} and confining stress, σ'_3, from 3 out of the 9 drained triaxial tests mentioned above. As it can be seen in Figure 4-4, the curve fit of the E_{50} profile with depth had a very good match with test data when omitting values from sample “Batch_1”, resulting in E_{50}^{ref}= 33 MPa.

From the total of the oedometer tests, only 2 out of the 9 constant rate of strain oedometer tests corresponded to sand unit Ib. Following the definition of E_{oed} by (Mylonas-Rontiris, 2018), the tangent stiffness for primary oedometer loading was measured in the reference lateral stress level, $p_{ref} = 100$ kPa. In both tests, this resulted in $E_{oed}^{ref} = 33$ MPa. However, using CPT data and the correlation found in (Robertson P., 2009) between constrained modulus and cone resistance, created the scatter plot of Figure 4-5. By omitting the sudden jump between 2-4 m depth, the red profile for E_{oed} was derived based on in-situ data. The design profile used in calculations was chosen the two extremes, closer to the laboratory test data, since the resulting value of $E_{oed}^{ref} = 40$ MPa was more consistent with the already calculated E_{50}^{ref} value.

Regarding the unloading/reloading reference stiffness E_{ur}^{ref}, the Plaxis manual suggests a value 3 times that of E_{50}^{ref} and equal to 99 MPa.

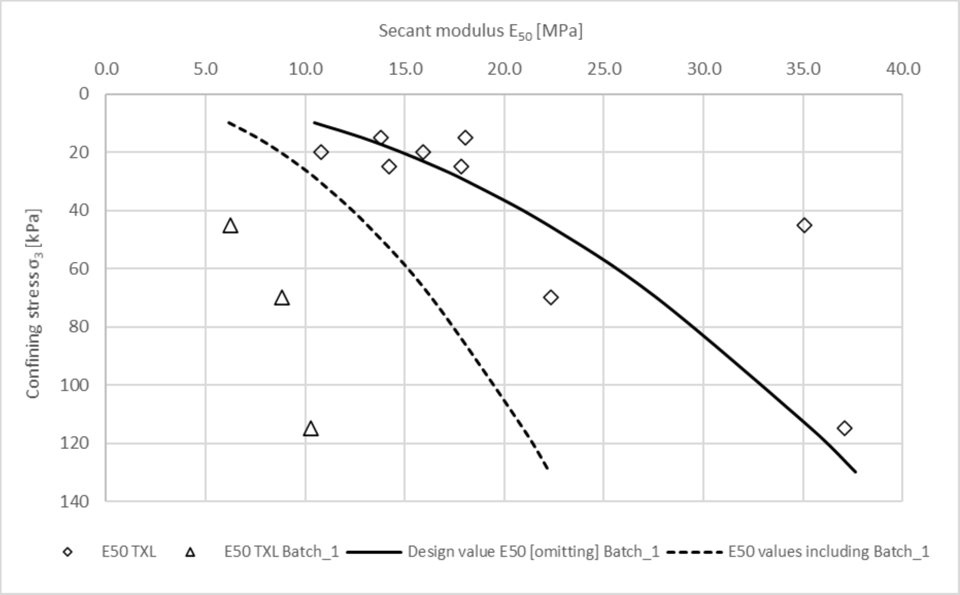

Figure 4-4 Curve fit of E_{50} modulus using scatter data from drained triaxial tests in sand.

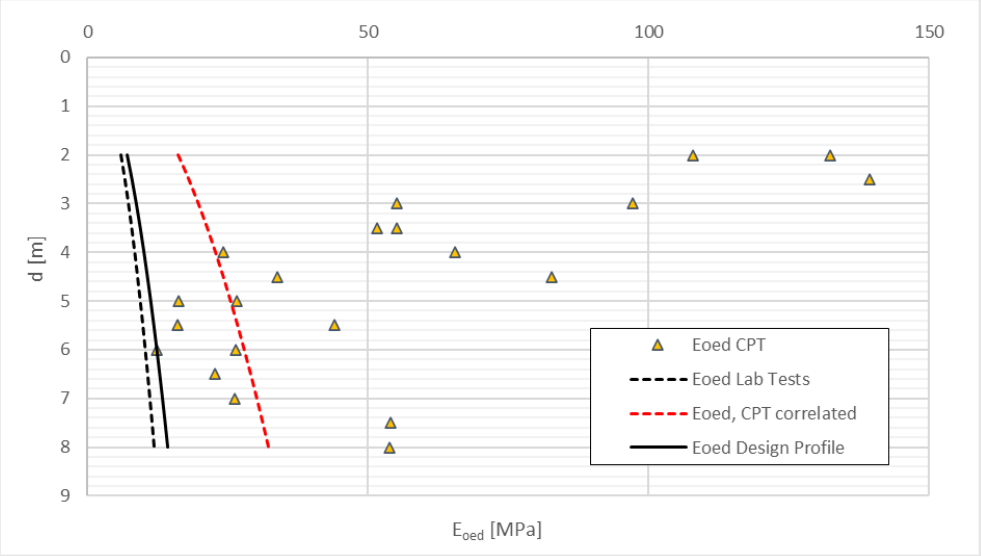

Figure 4-5 Curve fit of E_{oed} modulus using CPT scatter data and oedometer test data.

The parameter ν_{ur} was chosen equal to 0.2 after consulting with SPT Offshore geotechnical engineers, a value that additionally matches with the one used by SPT in their Plaxis sand model for AOWF (SPT Offshore, 2016).

For the calibration of the reference elastic shear modulus, the shear wave velocity data from the seismic cone penetration tests (SCPT) were used to create the scatter plot of Figure 4-6, according to Equation 4.17 (Ahmed, 2017):

$$G_0 = \frac{\gamma}{g} V_s^2 \tag{4.17}$$

After graphically selecting a representative G_0 profile with depth, the reference value G_0^{ref}=115 MPa was used for lateral stress $p_{ref} = 100$ kPa (27 m depth).

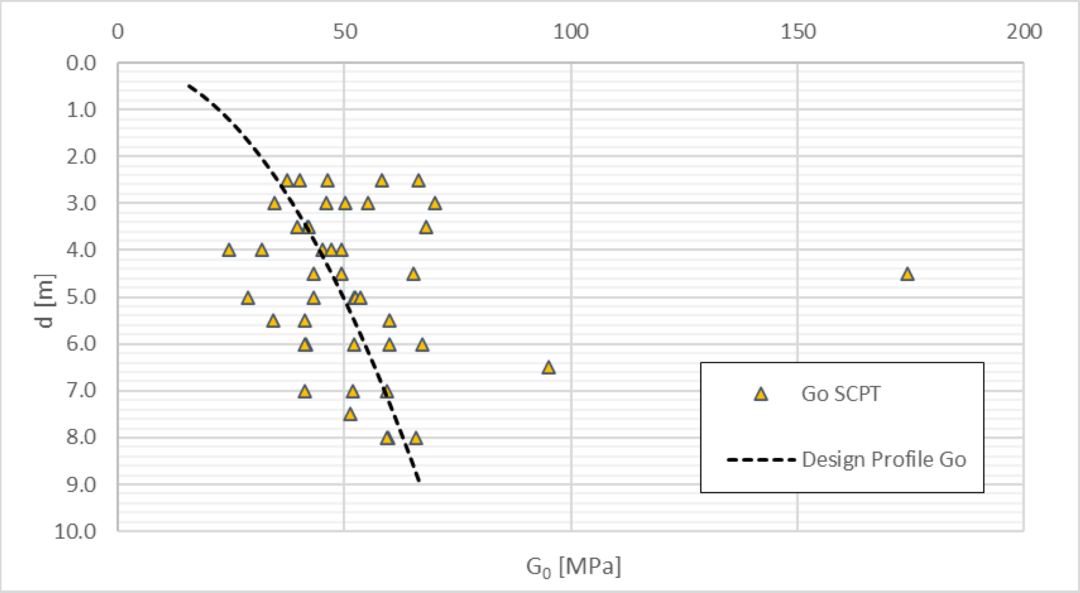

Figure 4-6 G_0 scatter plot as calculated using SCPT data and curve fit of G_0 design profile.

The parameter $\gamma_{0,7}$ controls the strain level at which the soil starts to lose its initial elastic shear stiffness but what it practically does, is affect the shape of the tail of the sigmoid hyperbolic function of Equation 4.14, the head of which is defined by G_0. Graphs of shear modulus versus shear strain were retrieved from two of the direct simple shear (DSS) tests that were corresponding to sand unit Ib. Their curves were similar and only one is presented here for clarity. Figure 4-7 shows the similar shape of the design profile, using a value of $\gamma_{0,7}$=5·10^{-5}, compared to that of the DSS tests.

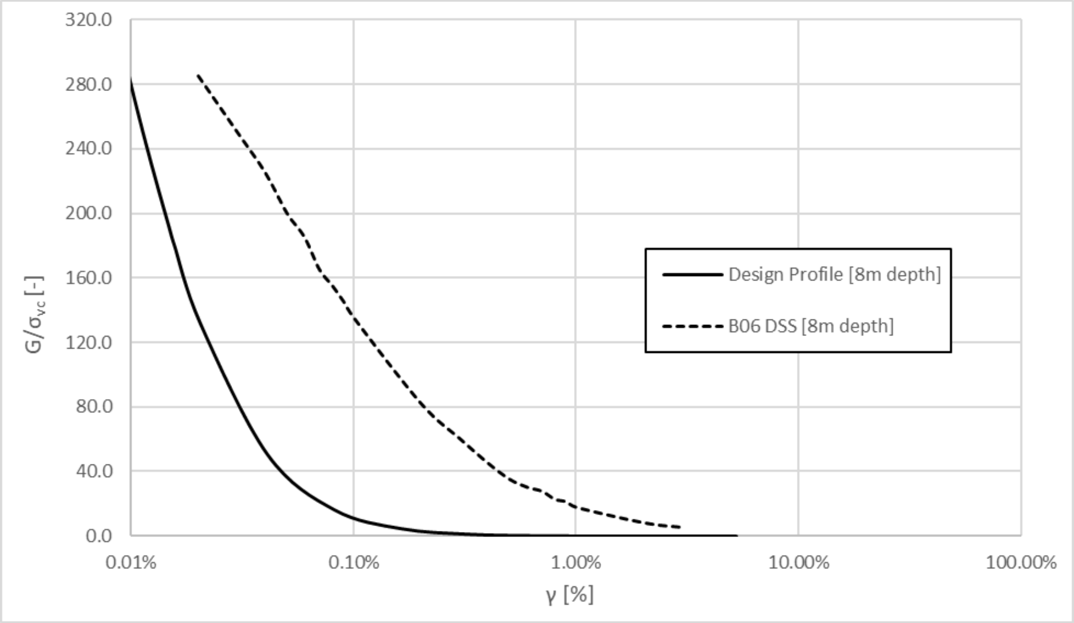

Figure 4-7 Evolution of shear modulus versus shear strain in DSS testing.

4.5.2 NGI-ADP

The NGI-ADP model will be used to simulate clay, and specifically soil unit II, as mentioned in section 4.1. The model parameters, according to the Plaxis 3D manual, are presented in Table 4-2:

Table 4-2 NGI-ADP input parameters.

γ_{sat}	Specific unit weight	18.9	[kN/m^3]
γ_f^C	Shear strain in triaxial compression	10.5	[%]
γ_f^E	Shear strain in triaxial extension	13.6	[%]
γ_f^{DSS}	Shear strain in direct simple shear	14.0	[%]
$s_u^{A,ref}$	Reference (plane strain) active shear strength	50	[kPa]
$s_{u,inc}^A$	Increase of shear strength with depth	2.75	[kPa/m]
s_u^P/s_u^A	Ratio of (plane strain) passive shear strength over (plane strain) active shear strength	0.83	[-]
s_u^{DSS}/s_u^A	Ratio of direct simple shear strength over (plane strain) active shear strength	0.95	[-]
G_{ur}/s_u^A	Ratio unloading/reloading shear modulus over (plane strain) active shear strength	552.4	[-]
τ_0/s_u^A	Initial mobilization	0.264	[-]
R_{inter}	Interface strength coefficient	0.77	[-]

The same specific unit weight γ_{sat} was used as in sand, equal to 18.9 kN/m^3. The shear strain values for failure in triaxial compression (TXC), extension (TXE) and direct simple shear (DSS), were derived from the unconsolidated and consolidated, triaxial compression and extension tests and direct simple shear tests, respectively, mentioned in section 4.2. In all tests, the shear strain at peak deviatoric stress was obtained and their values were averaged into those of Table 4-2.

Moreover, the aforementioned peak deviatoric stress values for TXC, TXE and DSS, were plotted against specimen depth as in Figure 4-8. Consecutively, the design profiles for s_u^A, s_u^P and s_u^{DSS} were derived graphically to accurately match the laboratory testing scatter data. Additional validation was provided by comparing said design profiles with the $s_{u,CPT}$ values resulting from in-situ CPT tests using Equation 4.18 (Robertson & Campanella, 1983), correlating undrained shear strength with cone resistance, q_c. Very good agreement with laboratory data was achieved using N_k value equal to 15, which is in line with literature (Lunne et al., 1976; Robertson & Campanella, 1983).

$$s_{u,CPT} = \frac{q_c - \sigma_0}{N_k} \tag{4.18}$$

The G_0 values over depth were retrieved from triaxial compression and extension tests with the addition of a bender element. The bender element allows the measurement of shear wave velocity and, thus, elastic shear modulus, within the specimen during triaxial loading. The G_0 design profile was then determined graphically as in Figure 4-9.

The initial mobilization τ_0 was calculated at depth $z = -10$ m, which coincides with the foot of the foundation (as described in later chapters). Using K_0 and ν values equal to 0.55 and 0.35, respectively, the τ_0/s_u^A ratio was calculated to equal 0.264 at 10 m depth.

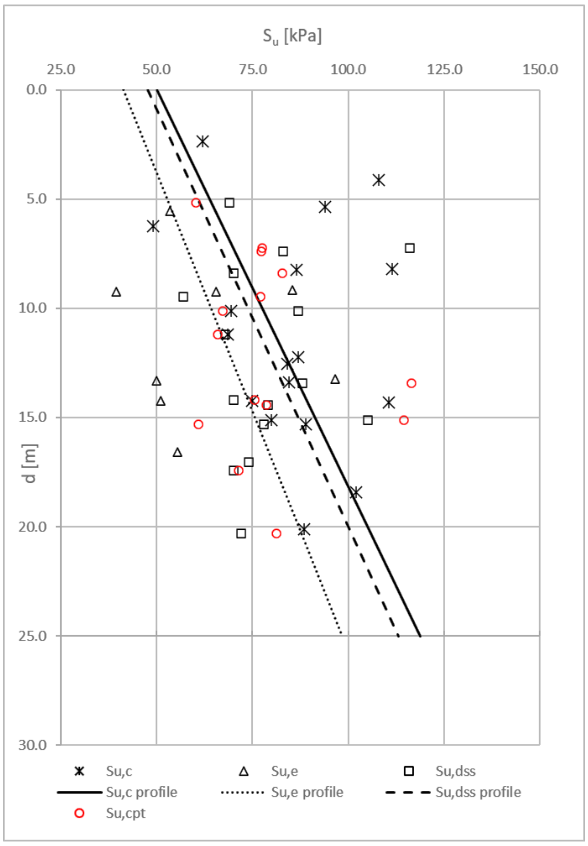

Figure 4-8 Scatter plot of undrained shear strength in TXC, TXE and DSS, as derived from respective laboratory testing, and undrained shear strength design profiles.

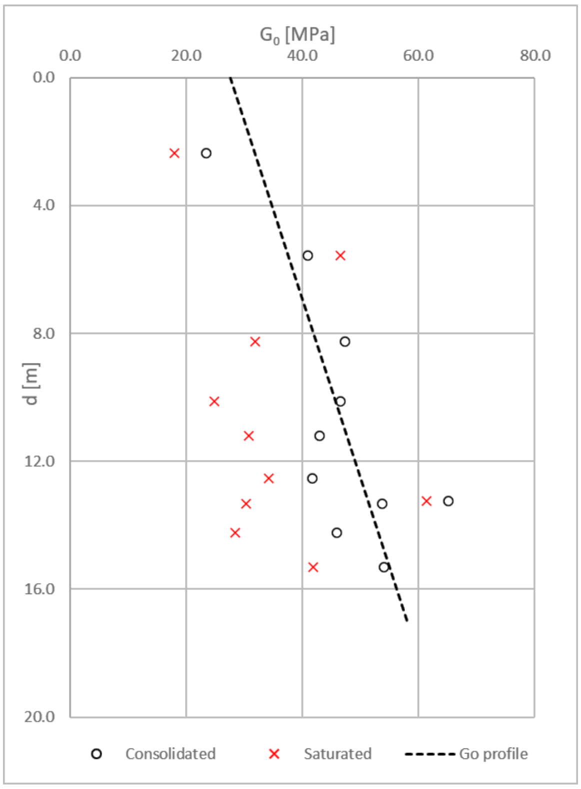

Figure 4-9 Scatter plot of shear modulus values as retrieved from triaxial testing with bender element and the corresponding design profile over depth.

4.6 Effect of Installation on Shaft Friction

The shearing imposed on the soil by the pile tip as well as the applied suction during installation, affect the in-place capacity of the foundation, more evidently on the shaft-soil interface. Moreover, in sands, loosening of the inner soil plug due to the upward water flow takes place, however, its effect will only be indirectly accounted for here, by using a different inner shaft friction coefficient.

4.6.1 Installation in Sand

The final input parameter for calculations was the interface coefficient, R_{inter}, which controls the strength reduction in soil-structure interfaces, compared to the rest of the soil. Generally, interface resistance in sands is expressed with the angle of external friction, δ, that is used in the MC failure criterion instead of φ and is correlated to shaft surface roughness. However, in suction foundations, the installation process affects the soil around the shafts of the caissons and special attention was given to this. The normal stress to the caisson shaft equals to:

$$\sigma'_h = \sigma'_v K_0 \tan(\delta) \qquad with \quad K_0 = 1 - \sin(\varphi) \tag{4.19}$$

With σ'_v being the acting vertical stress and K_0=0.426, the lateral stress coefficient. According to (Houlsby et al., 2005b), the term $K_0 \tan(\delta)$ cannot be separated and is equal to 0.70, while Hung et al. (2017) found a value equal to 0.85. In both cases, solving with respect to δ yields values of external larger than internal friction angle. Although this has no physical meaning whatsoever, it implies that after suction installation in sand, at least on the proximity of the external caisson shaft, there is a local increase of vertical stresses due to the downward water flow, which in turn cause an increase in normal stresses and shaft friction. That is not the case for the inside shaft of the caisson, where the water flow during installation is upward, thus, decreasing vertical stresses locally and Wang et al. (2019) suggest a reduction value between 0.55-0.85. As a result, an external interface coefficient, $R_{external}$, equal to 1.0 will be used ($\delta \geq \varphi$), and an internal one, $R_{internal}$, equal to 0.65, using the common relation of δ equal to 2/3 φ.

4.6.2 Installation in Clay

The skirt penetration during installation will reduce the shear strength of clay to the remoulded shear strength, $S_{u,rem} = S_{u,0}/S_t$, which is the original shear strength divided by the sensitivity (Andersen & Jostad, 2002). After installation, the clay shear strength along the skirts will increase with time due to dissipation of excess pore pressure, thus, normal effective stress increase, and thixotropy. The interaction in strength gains between the above is not certain and it is conservatively assumed that they occur independently and not additively (Andersen & Jostad, 2002).

Following a total stress analysis for clay, only the thixotropy effect will be considered. Thixotropy can be defined as the process of softening after remoulding, followed by a time dependent return to the original harder state under constant water content and porosity (Mitchell, 1960). The thixotropy strength ratio, $C_t = S_{u,t}/S_{u,rem}$, increases with time as well as plasticity index.

The average plasticity index I_p for unit II was found equal to 22% from the corresponding plasticity index tests (section 4.2). The sensitivity, S_t ,was found equal to 1.8, using fall cone test data as well as unconsolidated undrained triaxial test data (section 4.2), that compared remoulded to undisturbed shear strength for unit II. Using Equation 4.20 as in (Andersen & Jostad, 2004), the interface set-up factor, α, was calculated equal to 0.77, which corresponds to the model's interface strength factor R_{inter}. The above value corresponds to 3-month set-up effects, which is suitable for in-place capacity calculations.

$$\alpha = S_{u,t}/S_{u,0} = 1.4/S_t \qquad for \quad I_p < 30\% \tag{4.20}$$

5 Equivalent Monobucket - TSPC Dimensions

As mentioned in the literature review of section 1.5, despite lack of extensive research, there are indications that the behaviour of the clustered TSPC foundation is closer to that of mono-caisson than of an SBJ, which has also been confirmed after discussions with senior SPT Offshore engineers. Choo et al. (2006) compared a tripod foundation with a mono-caisson of equal total bucket area using the same embedment ratio. The same concept will be followed here as a starting point in determining realistic TSPC dimensions for the load and soil conditions of AOWF. Although design optimization is not one of the main goals of this thesis, analyses of a foundation configuration that mobilizes most of its capacity and approaches failure can be more informative than those of an overdesigned foundation.

5.1 VHM Envelope for Sand

Villalobos et al. (2009) presented results of combined loading experiments on suction foundations carried out on low relative density sand. This appears consistent with the AOWF sand input (loose to medium sand of 25-50% relative density) and appropriate for an initial estimate. In their interpretation of the results, they formulated a yield volume in the VHM space, subsequently normalized by the maximum vertical load, V_0, into a yield surface in the HM plane. This normalization is common in the framework of hardening plasticity, and the V component controls the size of the yield surfaces, while the H and M components its shape:

$$y = \left(\frac{H}{h_0 V_0}\right)^2 + \left(\frac{M}{2Rm_0 V_0}\right)^2 - 2e\frac{H}{h_0 V_0}\frac{M}{2Rm_0 V_0} - \beta_{12}^2\left(\frac{V}{V_0} + t_0\right)^{2\beta_1}\left(1 - \frac{V}{V_0}\right)^{2\beta_2} = 0 \qquad (5.1)$$

Where h_0 and m_0 are intersection parameters (H and M axes crossing point of the yield surface), e is an eccentricity parameter and β_1, β_2 and β_{12} are shape parameters to best fit the experimental data into Equation 5.1.

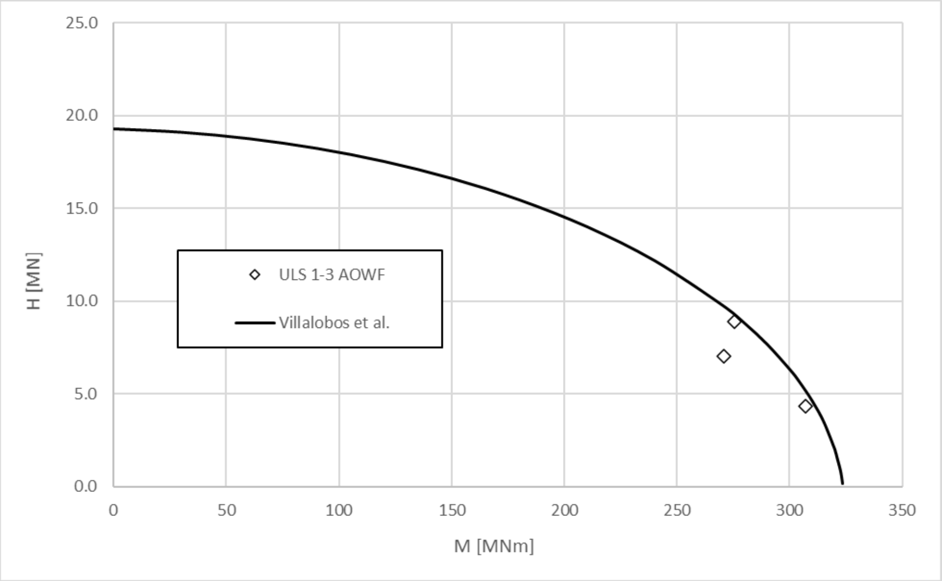

Figure 5-1 HM yield surface for an equivalent monobucket and the 3 ULS cases from AOWF.

The 3 individual TSPC buckets were assumed with an embedment ratio of one. The monobucket was given the same embedment length but with an area equal to the summation of the 3 individual buckets, thus, yielding an embedment ratio of $1/\sqrt{3}$=0.58. Villalobos et al. (2009) suggest values for the above parameters for L/D ratios of 0.5 and 1, of which the former was chosen since it is closer to the monobucket. The resulting HM yield surface depicted in Figure 5-1, along with the 3 ULS load combinations of section 3.3, correspond to a monobucket of 23 m diameter and 13 m embedment length. The resulting TSPC configuration, according to the above, is a cluster of 3 suction buckets of 13 m diameter, as well as embedment length. Additionally, it can be seen that, unlike the other two load cases, DLC 2.3, falls well inside the yield surface envelope, an indication that is not critical for design. As a result, it will be omitted in subsequent calculations.

5.2 Finite Element Verification

The above dimensions, however, after FEM verification, using the PLAXIS 3D model set-up described in the following chapter, both for the monobucket, as well as the TSPC, proved over-conservative. Figure 5-2 presents the lateral displacement and rotation exhibited by the foundation for different TSPC bucket diameters with a fixed centre-to-centre distance of 1.2 times the diameter, the smallest used in subsequent analyses. Naturally, for larger bucket distances of the same diameter, foundation displacements are expected to be even lower. By gradually dropping the size of the TSPC diameter up to 10 m, the foundation exhibited larger and larger displacements.

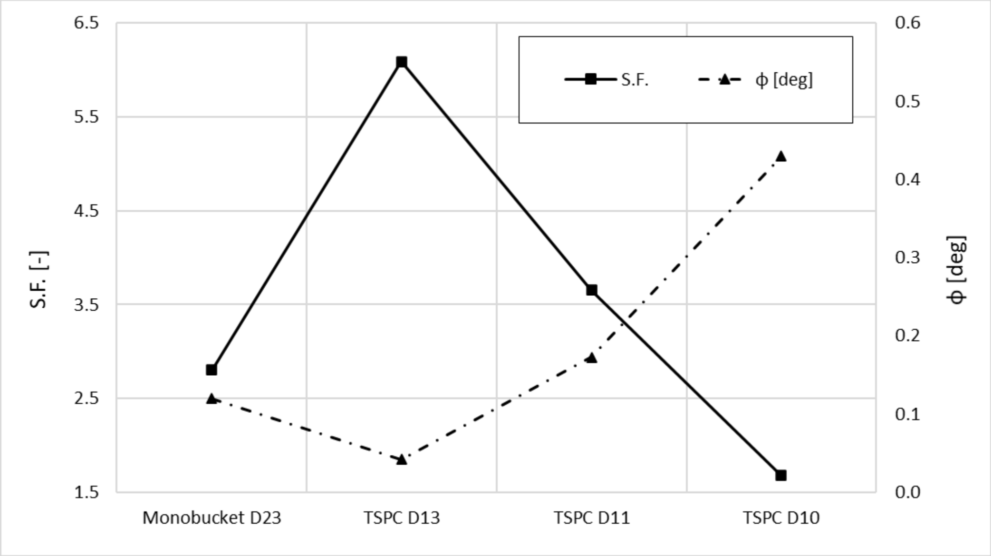

Figure 5-2 Lateral displacement and rotation of different TSPC configurations and the original monobucket.

The safety factor of the 10 m configuration was checked, using the relevant PLAXIS 3D analysis option (Bentley, 2020) and was found equal to 1.35 against the DLC 6.1 load case (design storm), which is a realistic value. Additionally, the 10 m diameter paired with 10 m embedment depth, fall within the dimensions used in the SBJs in AOWF:

Table 5-1 Comparison of adopted TSPC and AOWF SBJ bucket dimensions.

	D	L	
SBJ	9.5-10.5	7-12.5	[m]
TSPC	10	10	[m]

Conclusively, the above bucket dimensions will be kept fixed in the subsequent parametric analysis, where the parameters of interest will be the centre-to-centre distance, the soil type and the load combination

6 Parametric Analysis

The main purpose of this work is to improve the understanding of soil-structure interaction in the TSPC foundation. This was achieved by studying the effect of different geometrical configurations, soil types and load combinations on the acting failure mechanisms as well as the evolution of foundation stiffness. For that matter, a series of FEM analyses using PLAXIS 3D was conducted, and their results were interpreted. As described in chapter 4, two soil deposit cases were considered for analyses, a uniform sand, and a uniform clay layer, while two out of the three initial ULS load cases were used, as explained in chapter 5. Finally, five characteristic bucket centre-to-centre distances were considered, covering the spectrum of clustered TSPC configurations.

6.1 FE Model Calibration

Initially, the FE model and mesh had to be calibrated to minimize numerical inaccuracies, while maintaining optimal calculation times. For computational efficiency, only half of the foundation and soil deposit was modelled. This was made possible by the fact that in a tripod foundation, typically the most critical load direction coincides with either one of its 3 horizontal plane axes of symmetry so that one of the foundation feet is acting alone (usually in tension).

6.1.1 Model Size

The model dimensions were determined after consulting with senior SPT Offshore geotechnical engineers and determined as 8 times the bucket diameter (80 m) on either end of the x-axis as well as on the y-axis. The bedrock was assumed at -60 m, marking the z-axis boundary as in Figure 6-1:

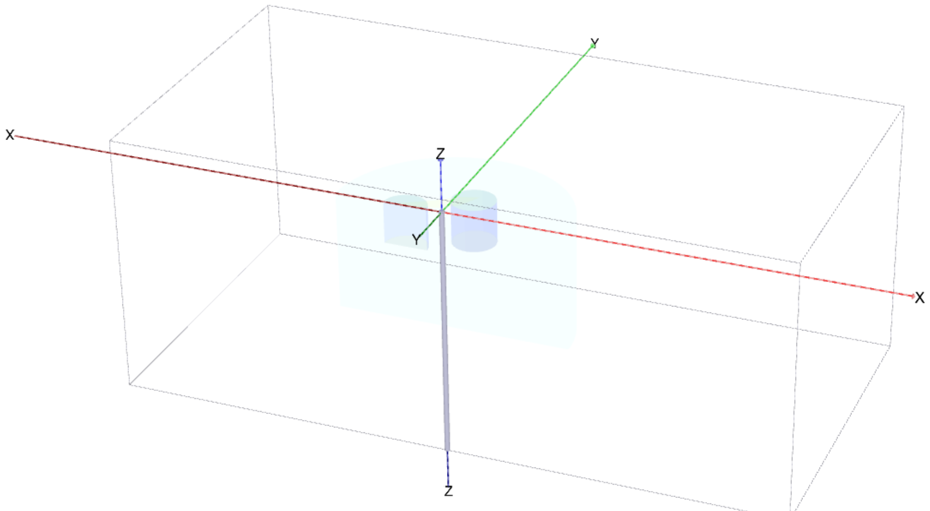

Figure 6-1 Model size and boundaries compared to suction bucket size.

The model dimensions were chosen so as to prevent load-induced excess stresses from reaching the boundary and triggering boundary reactions, that would, in turn, affect the response of the foundation by providing additional support to acting loads. The above model dimensions were verified by checking the extent of excess stresses in the model, and as can be seen in Figure 6-2, for the storm load DLC 6.1, the increase of relative shear stresses was contained within the model and away from the boundaries.

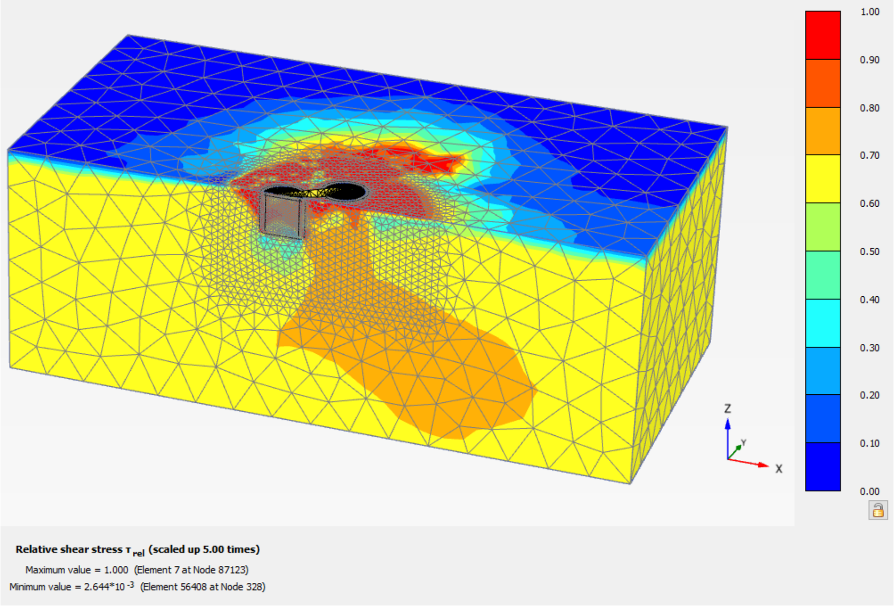

Relative shear stress τ_{rel} (scaled up 5.00 times)

Maximum value = 1.000 (Element 7 at Node 87123)

Minimum value = $2.644*10^{-3}$ (Element 56408 at Node 328)

Figure 6-2 Storm load-induced relative shear stresses contour plot as verification of model size.

6.1.2 Mesh Density

Another important FE model property was mesh density and local refinement. As it can be seen in Figure 6-3, the mesh was locally refined in regions of interest, with expected high-stress increments and plastic strains. A coarseness factor of 2 was used for the outer volume, close to the boundaries, a factor of 0.35 was used in the vicinity of the foundation and a factor 0.125 was used on the shafts of the caissons.

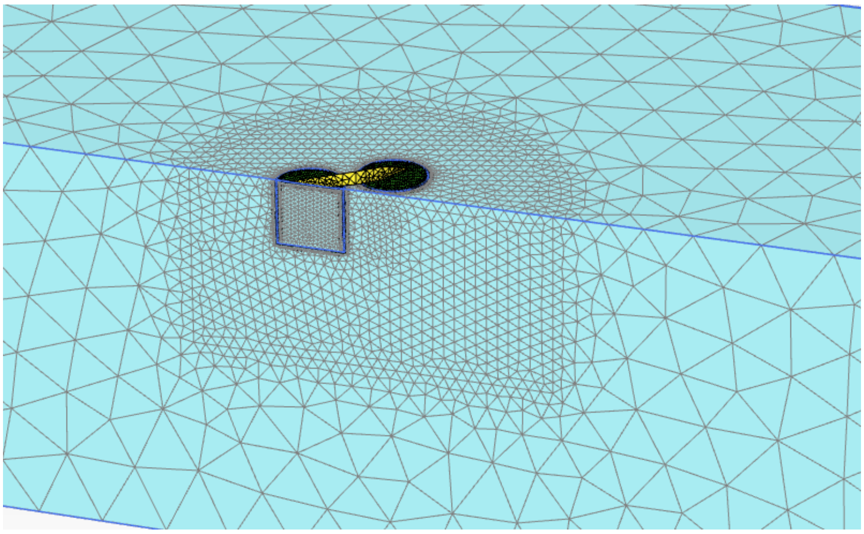

Figure 6-3 Mesh density and local refinement.

The final parameter chosen was the relative element size, which controls the global mesh refinement, while obeying relative local refinement options. To select its value, a sensitivity analysis was performed, comparing the resulting foundation rotation values for different relative element sizes. A very dense mesh, consisting of approximately 126.000 elements, was used as a reference, with the assumption that computational accuracy increases for a denser FE mesh. In Figure 6-4, it can be observed that after approximately 58.000 elements (and a corresponding relative element size of 0.55), a further increase in the number of elements, only marginally decreases deviation from the “accurate” dense mesh case.

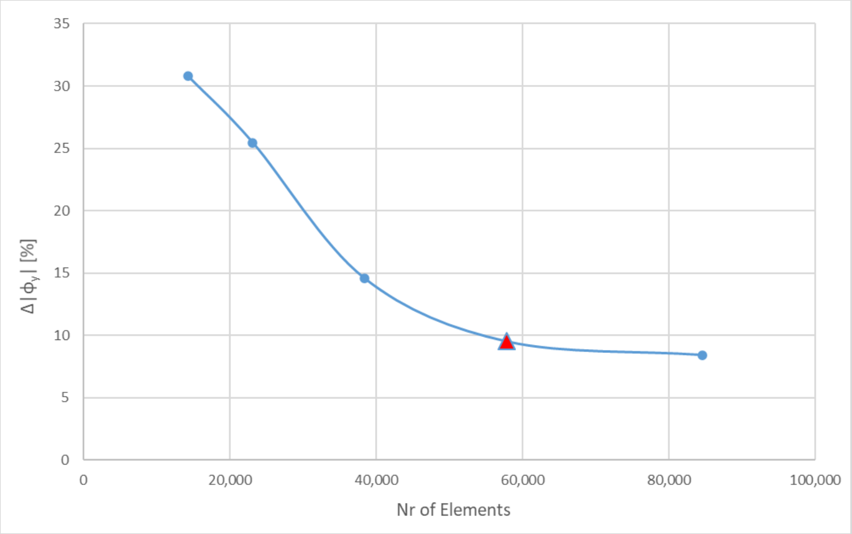

Figure 6-4 Deviation in the calculation of rotational angle between different mesh densities with respect to an “accurate” very dense mesh.

6.1.3 Foundation Model

Similar to the rest of the model, only half of the foundation was modelled, for computational efficiency. As explained earlier, the load direction coinciding with a horizontal symmetry axis of the foundation was deemed the most critical. To maintain symmetry over the x-z plane of the model, certain degrees of freedom of the foundation were bound, and specifically, displacement on the y-axis and rotation around the x-axis and z-axis.

The foundation was modelled using plates for the caisson shafts, and rigid bodies for the caisson lids and connection beams. As a result, connection flexibility was not considered in subsequent calculations. Interfaces were used for all soil-structure contact surfaces and, additionally, on the shear surfaces tangent to caisson footings. In clay specifically, the soil-structure interface at the top lid of the caissons was given close to zero strength, so that reverse end-bearing is not taken into account.

Finally, in all calculations, a single (half) caisson was located on the left side of the model, and two (one) caissons were located on the right side of the model, meaning that in clockwise loading direction, a single caisson was acting in tension and two in compression. All displacements, acting loads and soil reactions were considered with respect to the geometrical centre of the foundation footprint, coinciding with the origin of axes.

6.2 Sand

6.2.1 Centre-to-Centre Distance

The first point of reference for both soil types was the effect of clustering on the behaviour of the foundation, with a special focus on the mobilization, or not, of an inner soil plug between the TSPC buckets. For this matter, five different configurations were studied with centre-to-centre distances varying from 1.2 to 2.0 times the bucket diameter (10 m). Figure 6-5 presents lateral displacement and rotation versus bucket distance graphs, both for clockwise and counterclockwise load direction, for the storm ULS case (DLC 6.1):

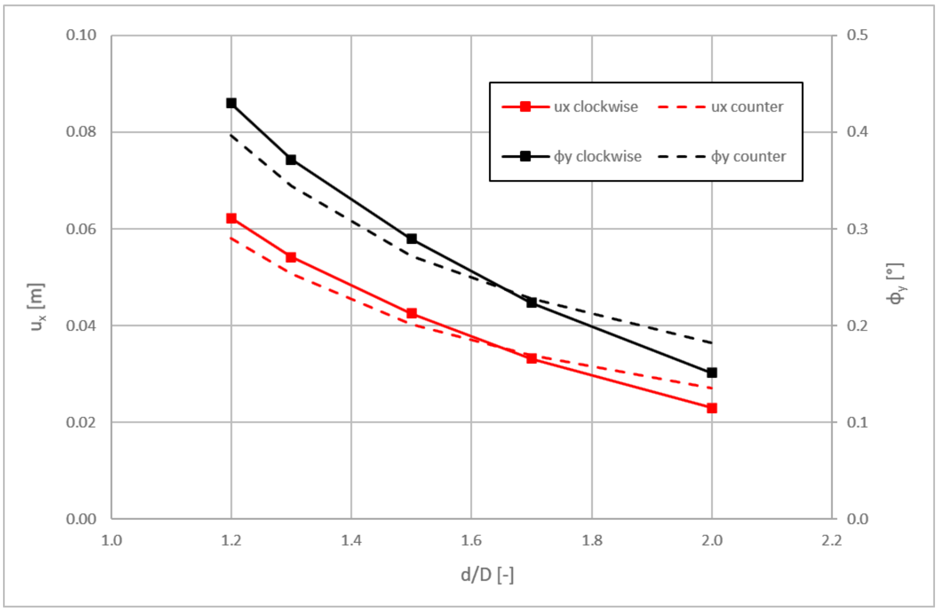

Figure 6-5 Lateral displacement and rotation for different bucket distances and load directions

Table C-5 in Appendix C presents the corresponding values of Figure 6-5, as well as the ones for DLC 3.2 (production load case). An interesting observation is that for the more clustered configurations, the clockwise load direction (one caisson in tension) yields higher displacements, as expected, but for larger bucket distances, the situation is reversed. This might, initially, look counter-intuitive, especially since sand has no tensile resistance. One possible explanation is the transition from a more clustered and scoop-type foundation response-failure mode to a more local, purely uplift-compressive response for larger distances (Figure 6-6). The combination of vertical superstructure load and the increase of acting axial load on the legs in compression could cause a more flexible “compressive” response, while the legs in tension are relieved under the combination of axial uplift load, due to overturning moment, and downward vertical load.

In Figure 6-6, one can easily observe that the scoop-type yield surface of the right is shared by both legs in compression in the 1.2D case, while in the 2.0D case, it is interrupted between the compressive legs and only demonstrates locally. This is an indication that, as expected, for larger bucket distances, the TSPC behaviour approaches that of an SBJ.

Of major importance is the determination of whether this evident interaction between TSPC buckets is beneficial or not. For that matter, the performance of the TSPC formation was compared with that of independent suction buckets (using superposition), in terms of foundation reactions to pure lateral and rotational displacements. Table 6-1 summarizes the reactions of the TSPC for different bucket distances, as well as those of single superimposed piles:

Table 6-1 Soil reactions against pure lateral and rotational displacements for the TSPC and single pile.

Displacement Control			**d/D**					**Single Pile**
			1.2	1.3	1.5	1.7	2.0	
|u_x|	0.025 [m]	**F_x** [MN]	19.4	20.1	21.2	22.1	23.3	23.5
|ϕ_y|	0.15 [°]	**M_y** [MNm]	191	202	222	242	271	187

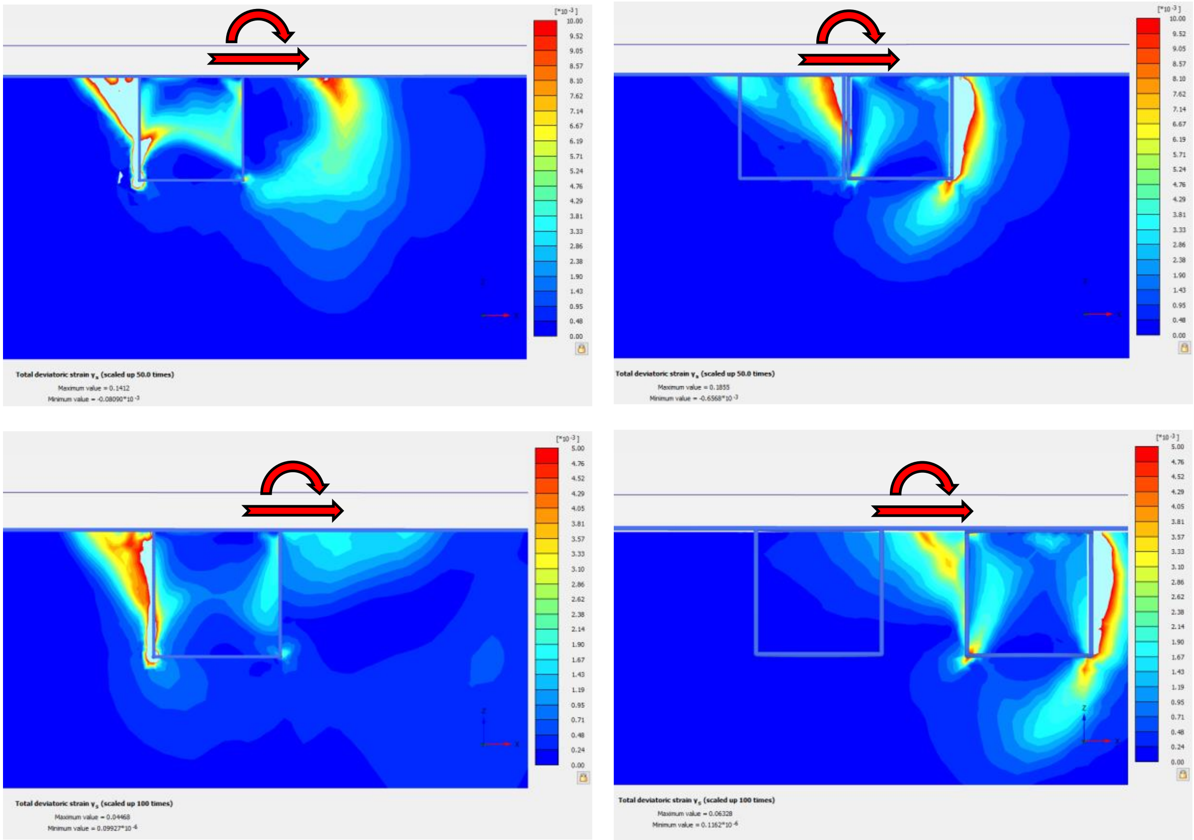

Figure 6-6 Comparison of shear strains for 1.2D and 2.0D bucket distances: (a) 1.2D tensile leg, (b) 1.2D compressive leg, (c) 2.0D tensile leg, and (d) 2.0D compressive leg.

Figure 6-7 illustrates the information in Table 6-1. It can be observed that for increasing centre-to-centre distances the lateral response of the TSPC is increasing asymptotically towards that of a single pile, while its rotational response is, normally, always larger than that of a single pile.

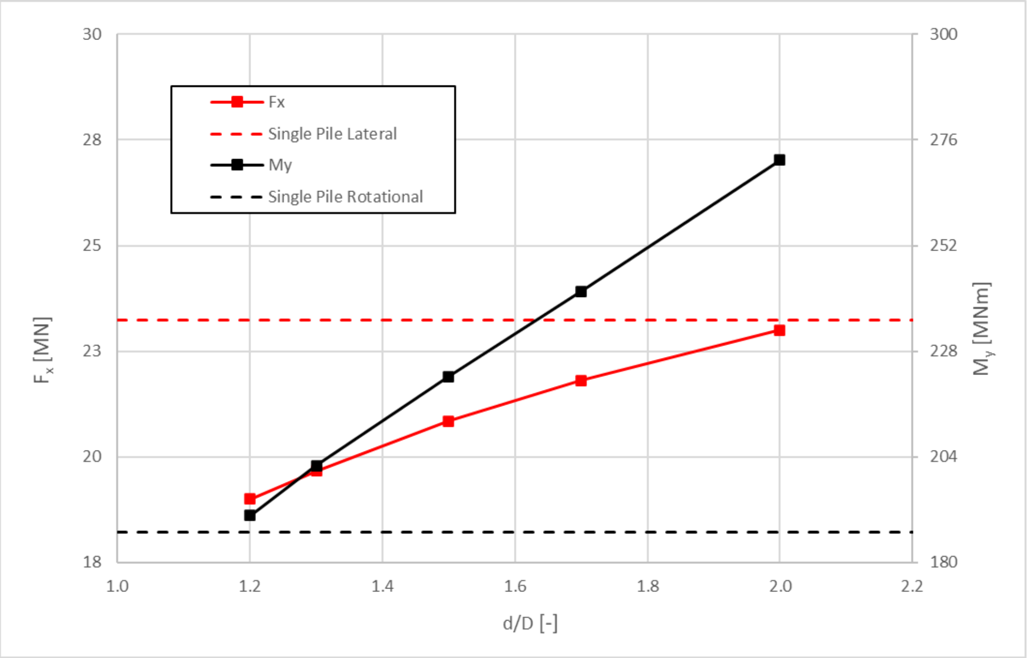

Figure 6-7 TSPC resistance against pure lateral and rotational displacement, compared to a single pile.

6.2.2 Failure Mechanism

The response of the foundation in sand under storm and production loading was very similar and the shear zone demonstrated in Figure 6-8 is representative of both cases. What is more interesting, though, is the different failure mechanisms triggered around the tensile (left) and compressive (right) leg. On the left shaft of the tensile leg an active failure wedge is forming, after the displacement of the foundation towards the right. The same mechanism is acting on the left shaft of the compressive leg (Figure 6-6) but is less evident because the major mechanism acting on the compressive legs is a deeper, scoop-like failure, more highlighted for clustered formations, as mentioned above. This is a clear indication that the compressive leg is providing most of its resistance through rotation, a phenomenon that is amplified for higher load levels.

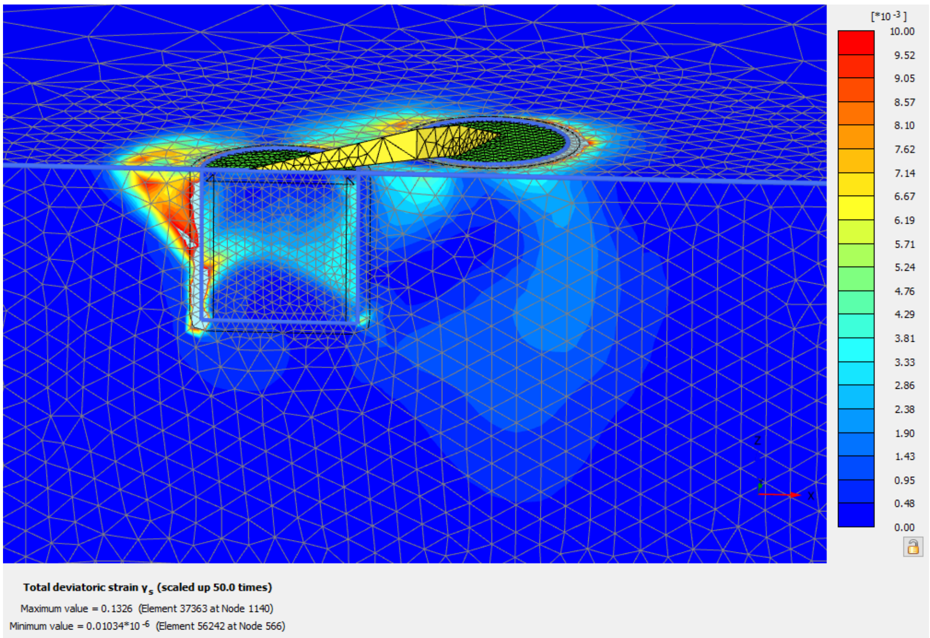

Total deviatoric strain γ_s (scaled up 50.0 times)

Maximum value = 0.1326 (Element 37363 at Node 1140)

Minimum value = $0.01034*10^{-6}$ (Element 56242 at Node 566)

Figure 6-8 Shear zone for 1.5D centre-to-centre distance in sand.

6.2.3 Centre of Rotation

Many of the above observations easily fit into the same narrative once the evolution of the foundation centre of rotation is studied. As mentioned above, initially the pair of uplift / downward forces acting on the tensile and compressive legs, respectively, has a favourable effect on the tensile leg by reducing the acting axial load (superposition with superstructure weight) and an unfavourable effect on the compressing leg by amplifying the effect of pre-existing vertical loads. The bearing capacity of a caisson in sand is, of course, much higher than its pull-out capacity, and as the moment load increases, it overcomes the effect of vertical superstructure load, and the tensile leg starts to fail in uplift, while the foundation starts to rotate around the compressive leg that starts to behave like an individual caisson (scoop-type failure mechanism). Indeed, Figure 6-9 illustrates the evolution of the centre of rotation from, initially, the tensile leg, to the compressive one. At which moment load level, the effect of the overturning moment pair will overcome the effect of the vertical load, depends on the geometrical configuration of the foundation. That, indeed, explains why for distances higher than 1.7D, the case with one leg in compression proved critical, for the specific load combination applied in all configurations. It should be noted, however, that regardless of load level, the centre of rotation remained at an approximately constant depth equal to 3/4 of the leg diameter, which is not in agreement with the assumption made in sector 2.1.5 for the NFA.

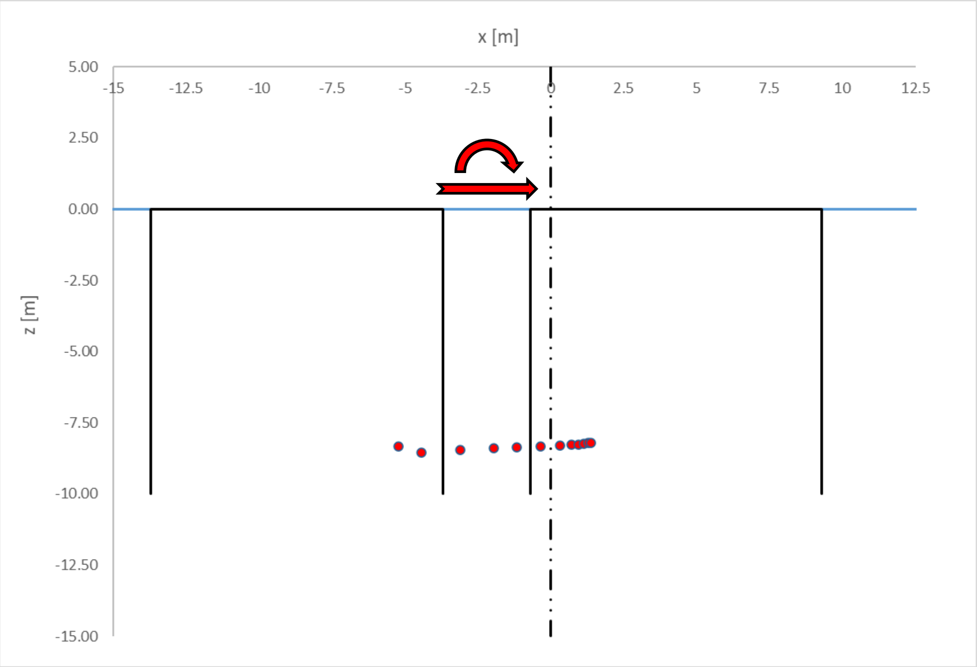

Figure 6-9 Evolution of the centre of rotation for clockwise loading in sand.

6.3 Clay

6.3.1 Centre-to-Centre Distance

Clay has a non-zero cohesion value, so unlike sand, can exhibit tensile strength and its shear resistance is not frictionally dependent on the stress state. As a result, the TSPC is expected to behave differently in clay and mobilize different failure mechanisms. Similar to the sand case, five different centre-to-centre distances were studied ranging from 1.2-2.0 times the caisson diameter D. Figure 6-10 presents lateral displacement versus bucket distance graphs for clockwise and counterclockwise loading or DLC 6.1:

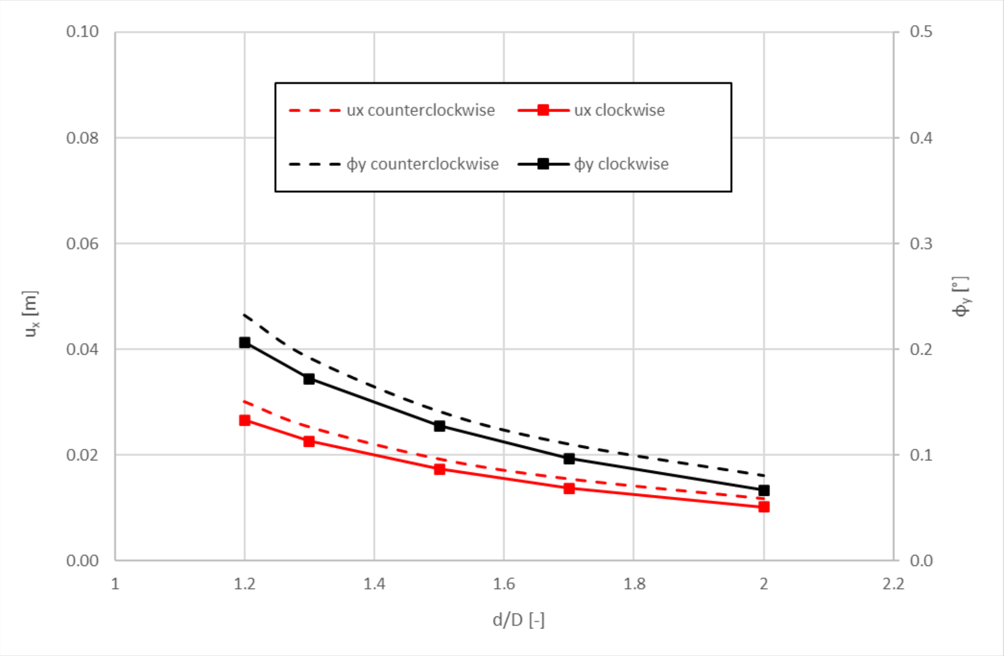

Figure 6-10 Lateral displacements and rotations versus bucket distance for two load directions.

Table C-6 in Appendix C presents the corresponding values of Figure 6-10 along with the ones for the rated wind speed load case (DLC 3.2). In contrast to the sand case, in all bucket distances, the case with one leg in compression proved critical. This is very interesting at first glance, especially since the bucket end-bearing capacity was not considered in calculations, and further investigation of the mobilized failure mode is necessary.

Additionally, a comparison was made between the performance of the TSPC foundation in pure lateral and rotational displacement and that of a single pile (linearly increasing its resistance to correspond to the 1.5 piles modelled in the TSPC). The displacement control parameters and the resulting soil reactions are summarized in Table 6-2:

Table 6-2 Comparison of TSPC and single pile for different bucket distances.

Displacement Control			**d/D**					**Single Pile**
			1.2	1.3	1.5	1.7	2.0	
$\lvert u_x \rvert$	-0.012	**F_x**	12.2	12.6	13.3	14.0	14.9	18.0
	[m]	[MN]						
$\lvert \phi_y \rvert$	-0.081	**M_y**	132	141	159	177	205	140
	[°]	[MNm]						

While Figure 6-11 illustrates what was already known from sand, i.e., that for larger distances the pure lateral resistance tends asymptotically to that of a single pile, its rotational stiffness is practically always higher.

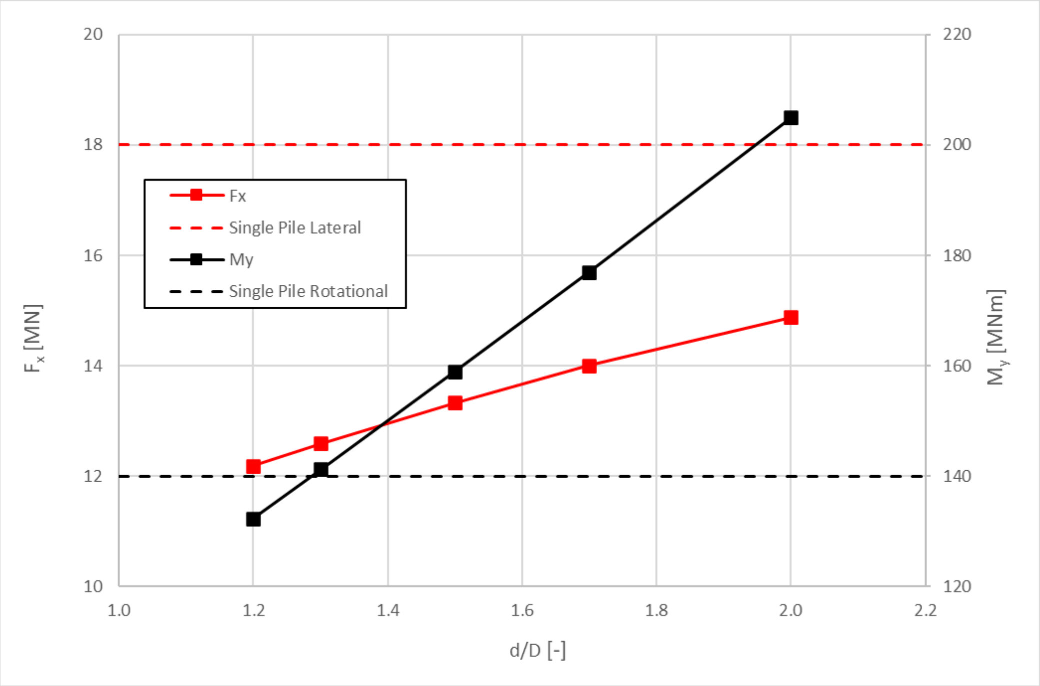

Figure 6-11 TSPC and single pile performance comparison.

6.3.2 Failure Mechanism

Furthermore, the effect of centre-to-centre distance on the development of an inner soil plug was investigated. Figures 6-12 and 6-13 compare the two extreme cases of 1.2 D and 2.0 D distances in terms of total displacements and shear strains:

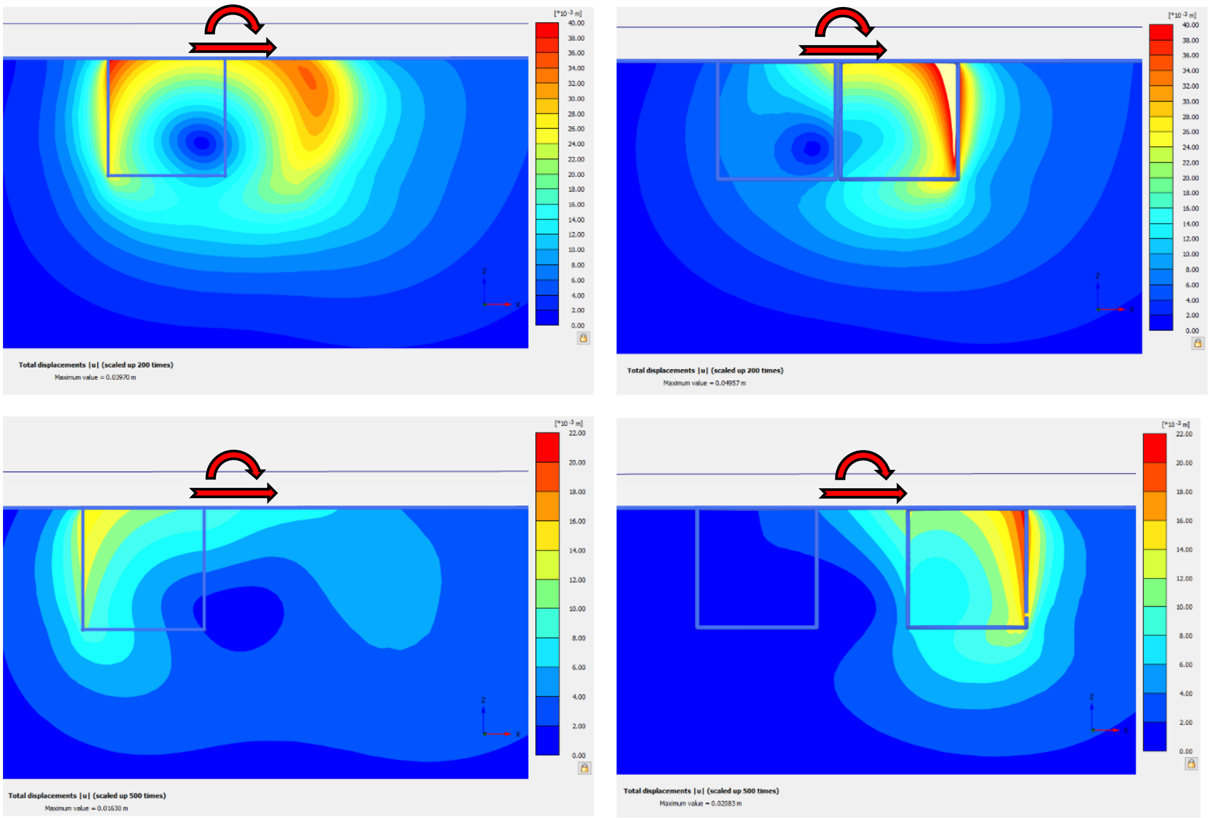

Figure 6-12 Total displacements for max. and min. bucket distance in clay: (a) 1.2D front foot (b) 1.2D rear foot (c) 2.0D front foot (d) 2.0D rear foot.

As it will be explained in section 6.3.3, the foundation centre of rotation coincides with that of the soil between the piles. The formation of an inner soil plug is emphasized for the more clustered formation. In the 2.0D case, there is also a tendency for an inner soil plug, but more local deformations start to develop, especially on the outer shafts of the caissons. Figures 6-13 (a) and (b) provides additional proof for the creation of an inner soil plug in the 1.2D case, with absent shear strains in the soil trapped between the piles, moving in conjunction with them, while a deep, global failure surface develops beneath the foundation. In Figures 6-13 (c) and (d), a triangular wedge of passive and active failure, respectively, can be observed on the inner shafts of the caissons. This, in combination with the vertical shear failure surface on the outside shafts, is reminiscent of the compressive caisson behaviour in sand, indicative of a more local failure as the distance increases.

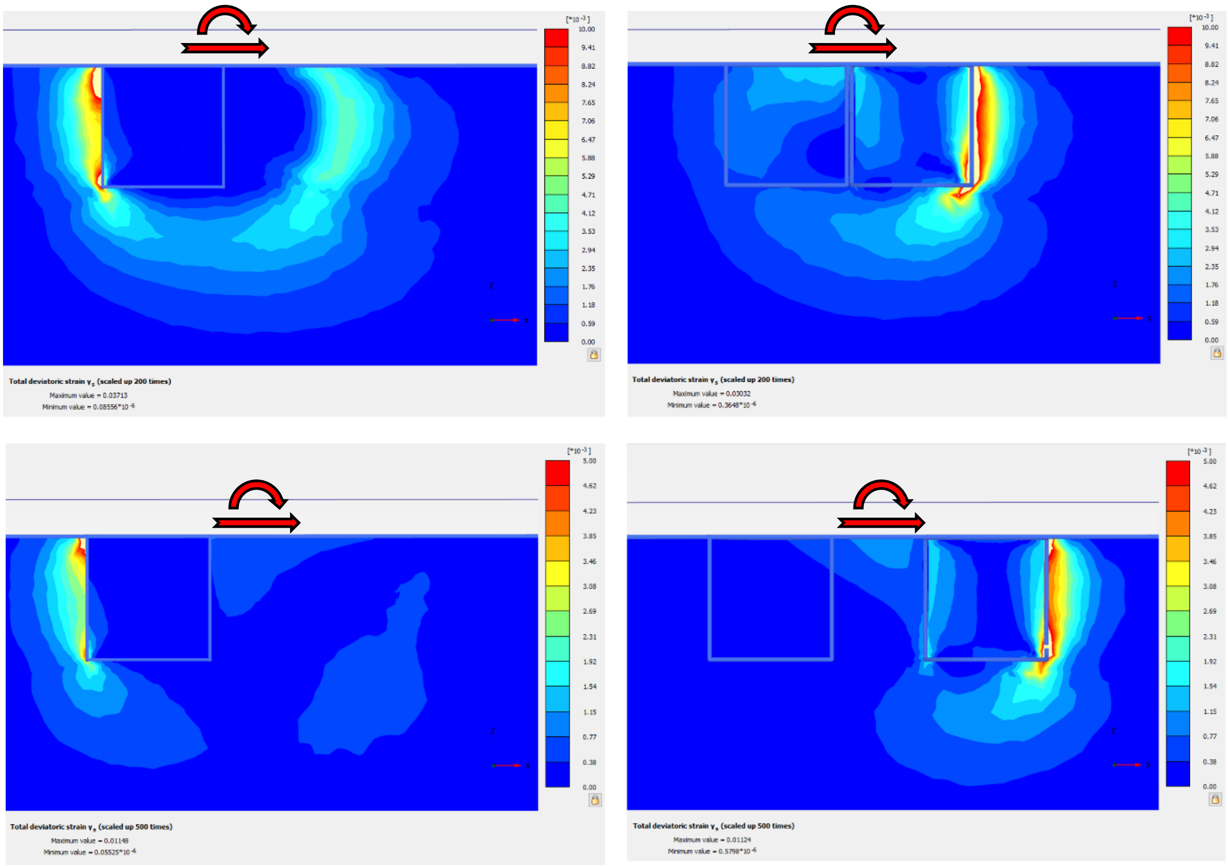

Figure 6-13 Shear strains for max. and min. bucket distance in clay: (a) 1.2D front foot (b) 1.2D rear foot (c) 2.0D front foot (d) 2.0D rear foot.

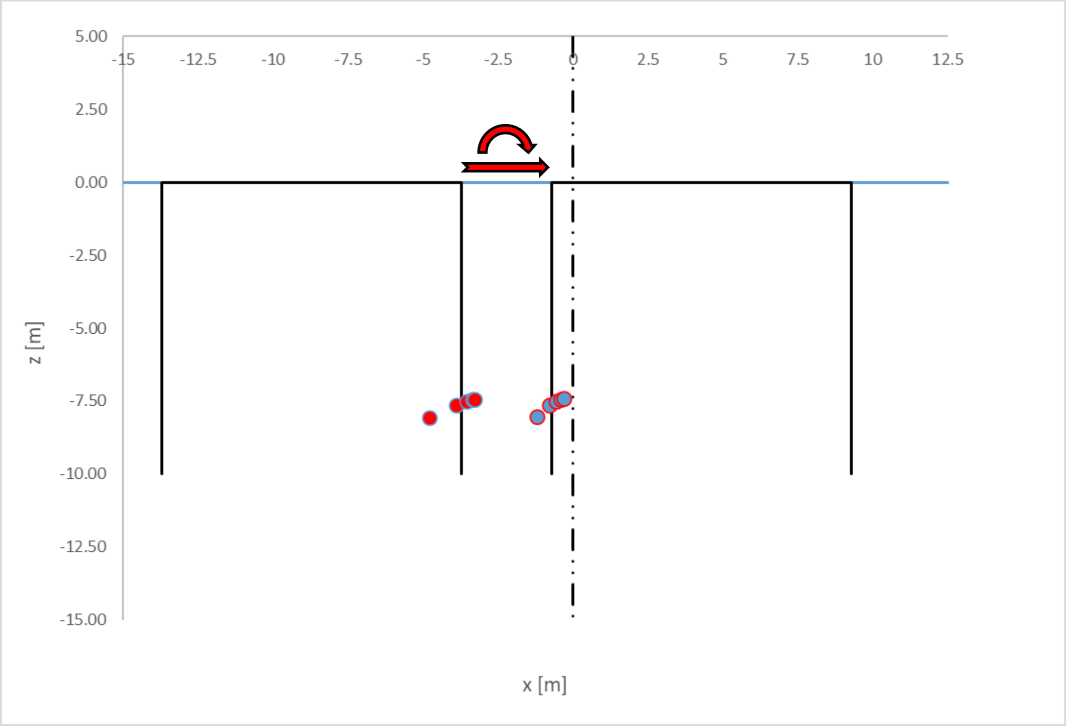

Figure 6-14 Rotation centre evolution for VHM (left) and HM (right) clockwise loading.

6.3.3 Centre of Rotation

The determination of the foundation centre of rotation proved very useful in interpreting the results of the clay analyses as well. An intermediate distance of 1.5D was used, to be as representative as possible. Figure 6-14 illustrates the evolution of the rotation centre for two types of loading. The centre cloud on the left "tensile" leg corresponds to storm DLC 6.1 VHM loading, while the cloud on the right "compressive" feet corresponds to storm HM loading in the absence of vertical loading.

One key observation, in accordance with strain and displacement plots, is that the TSPC in clay, especially for clustered formations, behaves as a unit along with surrounding soil, rendering it practically similar to a monobucket with a diameter equal to the overall foundation footprint. The individual piles only partially mobilize their bearing capacity in compression and pull-out capacity in tension, but primarily rotate in place, using the active and passive resistance of their shafts to move surrounding soil and force a global failure mode, beneath their footings. As a result, neither side of the foundation is expected to behave stiffer in pure HM excitation (see Figure 6-14) if the load is applied above the centre of gravity (as is the case here). The presence of vertical load, however, partially relieves the "tensile" part of the foundation and further plastifies the "compressive" one, displacing the rotation centre as in Figure 6-14. Similarly to loading in sand, the centre of rotation remains roughly at a depth equal to 3/4 times the leg diameter, rendering the mudline level assumption rather unconservative.

6.4 Eccentricity

A modelling weakness of the followed approach in this work is the application of the vertical load V on the mudline level, instead of the centre of mass of the superstructure. Consequently, once the foundation and, thus, the superstructure starts tilting, the additional overturning moment due to vertical load eccentricity is not taken into consideration. In terms of foundation capacity, this can easily be overcome through the iterative process described below using load-displacement curves for overturning moment and rotation. However, the effect of eccentricity on foundation stiffness cannot be captured without proper modelling of the superstructure and application of its weight on the centre of mass.

According to Tables C-5 and C-6, the largest rotation angle was found in the 1.2D bucket distance configuration under storm loading in sand and equal to 0.430 degrees, with the same configuration under production loading yielding the second-largest rotational angle of 0.417 degrees. These two cases were tested by iteratively updating the moment load acting on the foundation due to increasing rotation angle. By using extended load-displacement curves, an increase of about 5% and 3% was calculated for rotational angle and overturning moment, respectively.

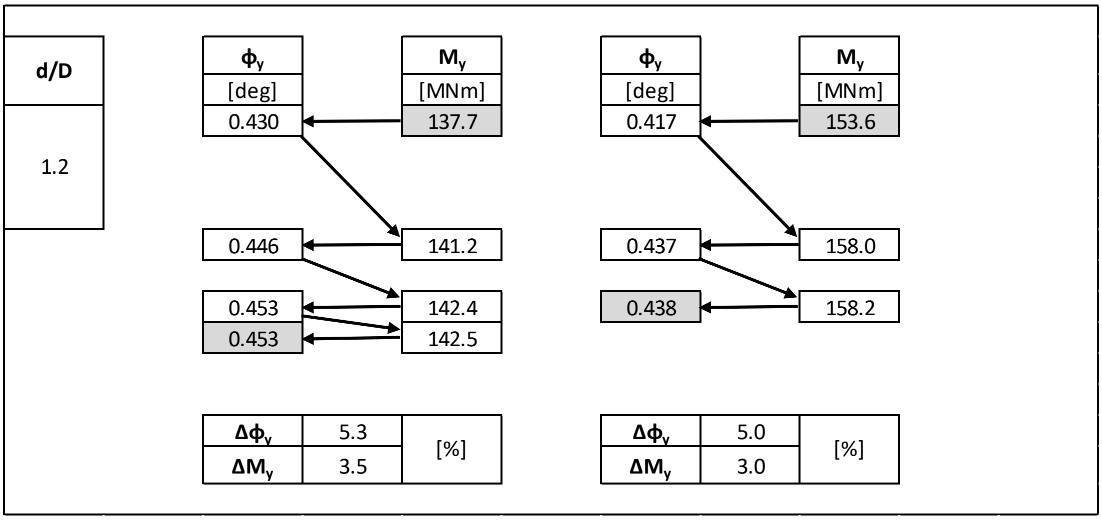

Figure 6-15 Calculation of additional overturning moment and rotation due to vertical load eccentricity.

6.5 Load Effects

An important task in this work was the investigation of foundation stiffness evolution for different load levels and load combinations. This section will critically discuss the results summarized in Appendix D.

6.5.1 Load Displacement Curves

Figure D-1 shows that in sand, the lateral and rotational stiffness of the TSPC foundation is very sensitive to bucket distance (see also Figure 6-7). Moreover, this sensitivity is emphasized in the lateral stiffness for the storm load case (higher horizontal load) and in the rotational stiffness in the rated wind speed load case (higher overturning moment). It can also be seen, that for clustered formations (smaller d/D ratio), the elastic stiffness is lost almost immediately (at around 20% of the acting load) for both load cases. This characteristic yielding of the soil-foundation system can be explained by the plastic hardening and consecutive yield surfaces of the HSM, used in the analyses, allowing for a smooth transition from elasticity to plastic failure.

In lateral and rotational load-displacement curves, a common trend can be observed in clay for both load cases. Specifically, the distinct segregation of the graph into two branches, one with elastic (initial) stiffness, and one where considerable and abrupt stiffness reduction takes place (Figure D-2). The breakpoint is around 30% of the maximum applied load. A potential explanation for this could be the sudden loss of frictional resistance on the shafts of the tensile caisson, once the S_u^{DSS} limit of the interface is reached, leading to a significant reduction of its contribution to foundation resistance. Additionally, contrary to sand, the load-displacement curves for clay appear to have a somewhat bi-linear or less emphatically yielding shape.

6.5.2 Stiffness Evolution

As expected, the larger pile distance configurations exhibit a much stiffer behaviour, especially for smaller deformations and load levels. This might be of special interest in cyclic or fatigue analyses, where strain accumulation is of interest for the design. In the secant stiffness evolution graphs, the observation of a gradual stiffness decay in sand and a bi-linear, brittle, response in clay, is confirmed. However, due to the scale of the graphs in Figures D-1 and D-2, direct quantitative comparison between sand and clay is not possible.

Figures D-3 and D-4 present the behaviour of the same configuration (1.5 D centre-to-centre distance) for sand and clay together. Two interesting observations can be made. Firstly, it is confirmed that the foundation in clay has a very high initial secant stiffness compared to sand. Secondly, the secant lateral stiffness, K_H, in both sand and clay is higher for the load case with the higher lateral load (storm). Similarly, but less emphasized, the secant rotational stiffness, K_M, is higher for the load case with the higher overturning moment (rated wind speed). This looks counter-intuitive from an initial perspective, since one would expect a more yielding response in the deformation parameter corresponding to the amplified load component (H or M) in each case. An explanation to the above, is partially, the fact that the horizontal displacement values are measured on the mudline level. Because the foundation centre of rotation is below the mudline, the rotation due to high overturning moments in the rated load case is disproportionately increasing mudline lateral displacements, even for smaller horizontal load. This can be viewed as proof of the heavy coupling between the two in-plane foundation stiffnesses.

7 Conclusions and Recommendations

The main objective of this thesis was to improve the understanding of soil-structure interaction in the TSPC foundation. This was achieved by identifying and focusing on key parameters, affecting the behaviour of the foundation and the soil around it, and investigating their contribution.

7.1 Conclusions

The effect of centre-to-centre distance was assessed both on the developing failure mechanisms and on the stiffness of the foundation. Its contribution was evident both in sand and in clay, with larger distances triggering more localized failure zones, around the shafts of the caissons, while more clustered configurations favouring the development of an inner soil plug between the TSPC legs leading to more global failure surfaces, beneath the foundation (scoop-type). The formation of the inner soil plug was more evident in clay but with indications of it in sand as well, in the lower end of centre-to-centre distances (1.2 D).

The effect of load level and load combination on foundation stiffness and failure mechanisms was also investigated. Initially, the foundation behaves elastically but with the increase of load level it starts to yield, with a loss of stiffness, either through yielding plasticity in sand or a more abrupt, brittle manner in clay. Additionally, for low load levels, far from the bearing capacities of individual caissons, only local shear zones are exhibited, restricted close to the shafts. Consecutively, with increasing loads, more voluminous shear zones appear, and global failure modes are triggered.

The different failure mechanisms in sand and clay were also studied. In sand, the failure modes were in principle local, e.g., active and passive failure wedges, and more importantly, could differ between the individual TSPC legs, even for clustered formations. On the contrary, in clay the foundation showed the tendency to behave as a unit, incorporating parts of the surrounding soil as well (inner soil plug, deep shear failure surfaces). Only on the upper end of centre-to-centre distances in clay, did the foundation begin to show signs of more localized failures mechanisms.

Finally, on many occasions, the TSPC was quantitatively and qualitatively compared to the SBJ and the monobucket. During design considerations, data from the SBJ case of AOWF, e.g., maximum lateral load and overturning moment or caisson diameter, was used as verification for the TSPC. The actual in-place behaviour of the TSPC, as it occurs from conducted analyses, in some cases resembles more that of a monobucket, while in others that of the SBJ. A very important distinction with the latter is the rotational displacement of individual caissons in the TSPC foundation, making their in-place behaviour more complex. In more general terms, the TSPC in clay behaved closer to a monobucket, while in sand, it exhibited certain similarities with the SBJ, like the use of torque resistance moment deriving from axial loads on the caissons.

7.2 Future Research

The following research recommendations aim to frame the work carried out in this thesis and provide insight on the effect of its intrinsic limitations and the assumptions made by the author.

In this research, only one value of embedment ratio (1.0) was used to investigate soil-structure interaction, regardless of soil type, and chosen to match the theoretical upper installability ratio for sand. Using the knowledge acquired regarding local and global failure mechanisms, further study is necessary towards the optimization of TSPC designs for site-specific sandy, clayey, or layered soils, investigating different embedment ratio and diameter values.

A quantitative formulation of steel and fabrication costs for the pile connection beams would, in conjunction with varying diameter and centre-to-centre distance, be the first step to an actual TSPC design optimization process since it would allow for the effective comparison of gains and losses in increasing the distance between the suction piles.

Moreover, the TSPC is a concept that, according to the writer, heavily favours an integral design approach for the support structure, i.e., foundation, transition piece, and tower of a WTG. Such an approach could make significant gains on computational time and efficiency of the overall structure, even assuming an interface with the WTG manufacturer at the tower level since the support structure dimensions heavily influence the acting environmental (hydrodynamic) loads on the foundation.

Especially in terms of dynamic analysis and natural frequency, the inclusion of foundation as an essential part of the support structure during calculations can accelerate the iterative process by removing the additional uncertainty of foundation stiffness. This was an inherent limitation of this thesis, since the luxury of an iterative geotechnical (foundation stiffness) and structural (central column dimensions) design, was not available and only the initial estimate of mudline fully clamped behaviour was used, which later proved to be inaccurate (centre of rotation approximately at 3/4 times the diameter below mudline level).

Furthermore, the use of advanced constitutive soil models, i.e., HSMss and NGI-ADP, for the FEM analyses in this thesis was made possible by the vast amount of laboratory and in-situ test data provided to SPT Offshore by the end client in the AOWF project. Often, however, the available soil data for design can be limited to in-situ CPT tests and the choice of input soil parameters is made using empirical or area specific cone resistance relations. In combination with the added uncertainty that stems from a high number of input parameters, an investigation of the TSPC behaviour using a simpler, industry friendly, constitutive model, like the Mohr-Coulomb, is a fair suggestion. This would, additionally, facilitate the comparison and validation of the chosen FE model against small or full-scale test data available in the literature, a process which can prove to be more cumbersome when using advanced models.

Due to time scarcity and model complexity, a cyclic analysis was not possible in the scope of this thesis, and as a result, is suggested for future research, being very relevant for WTG foundations. Moreover, it was shown in this work that the pile proximity in the TSPC clustered formation affects the development of shear strains around the interacting piles. Thus, time-domain analyses with soil models capable of simulating hysteretic damping would be of interest in order to investigate the effect of pile-pile interaction on the foundation response to dynamic loads, especially since the wind industry is expanding into seismically active regions.

Additionally, the potential phase difference between wind and wave dynamic loading can apply opposing moment and lateral force pairs on a caisson foundation, thus, triggering more favourable failure mechanisms (compared to conventional WTF foundations), like the “reverse pendulum” (Karapiperis & Gerolymos, 2014). As a result, another potential would be to expand the work of Karapiperis and Gerolymos for static loading of monocaissons into dynamic loading of clustered TSPC foundations, utilizing similar VHM failure envelopes.

Finally, in this work, a rigid pile head connection and top plate was assumed to reduce modelling complexity and computational time, but also to investigate the effect of more global failure mechanisms, like the inner soil plug. However, this is an idealized case, and the incorporation of structural yielding, either in the TSPC connection beams or the caisson lid plate, is strongly suggested for future study to access its effect both on the response of the foundation and structural fatigue accumulation.

A Soil Unit Description

Table A-1 Geotechnical and geological description of soil formations.

Formation	Unit	General Description	Deposition Environment
Forth Formation	Ib	Very loose to medium dense silty SAND	Marine
St Abbs Formation	II	Soft to very stiff slightly sandy CLAY, with thin laminae to thin beds of silt and sand	Glaciomarine
Wee Bankie Formation	III	Firm to very stiff slightly gravelly CLAY, with thick laminae to thin beds of sand	Glacial

Table A-2 Soil layers on laboratory test data sampling.

Location	Unit	Top of layer [Mbml]	Base of layer [Mbml]	Soil type	Cohesion
A02	Ia	0.0	2.0	SAND	Non-cohesive
	II+III	0.2	20.0	CLAY	Cohesive
BO2	Ia	0.0	2.0	SAND	Non-cohesive
	Ib	2.0	6.0	SAND	Non-cohesive
	II+III	6.0	20.0	CLAY	Cohesive
BO6	Ia	0.0	2.0	SAND	Non-cohesive
	Ib	2.0	8.0	SAND	Non-cohesive
	II+III	8.0	20.0	CLAY	Cohesive

B Laboratory Test Overview

Table B-3 Laboratory Test Codes and Unit Distribution.

Unit	A02	B02	B06
Ib		6UUD, 3BagA, 3BagA	BATCH, BATCH_1, BATCH, BATCH_1, BATCH, BATCH_1, BATCH (4)
II + III	7UU, 12UU, 5WaxB, 6WaxC, 9WaxB, 14WaxC, 15WaxC, 3WaxC, 12WaxB, 10WaxB, 6WaxD, 14WaxB, 24BagA, 10WaxB, 14WaxB, 3WaxC ,6WaxC, 8WaxB, 12WaxB, 15WaxC, 3WaxC ,6WaxC, 8WaxB, 10WaxB, 12WaxB, 14WaxB, 15WaxC, 6WaxB, 8WaxB, 8WaxC, 9WaxC, 11WaxA, 14WaxC, 16WaxA, 8WaxC (2), 9WaxC (4)	10UUC, 15UUD, 7WaxB, 13WaxB, 16WaxA, 19WaxC, 9WaxB, 10WaxB, 15WaxB, 8WaxB, 11WaxB, 8WaxC, 9WaxC, 7WaxB, 14WaxC, 19WaxB, 9WaxB, 13WaxB, 17WaxC, 7WaxB, 9WaxB, 13WaxB, 17WaxC, 12WaxB, 15WaxB, 15WaxC, 16WaxB, 18WaxC, 15WaxC (2), 16WaxB (3)	12UUD, 15UUC, 17UUC, 20UUB, 23UUD, 15WaxB, 21WaxB, BATCH, BATCH_1, 11WaxA, 13WaxC, 16WaxD, 10WaxB, 17WaxD, BATCH_2, 14WaxC, 10WaxB, 15WaxB, 12WaxD, 16WaxD, 18TubeA, 10WaxB, 12WaxD, 15WaxB, 16WaxD, 18WaxA, 10WaxC, 18WaxC, 21WaxC

Table B-4 Laboratory Test Colour Legend.

Unconsolidated Undrained Triaxial (11)	Anisotropically Consolidated Undrained Triaxial Extension (4)	Isotropically Consolidated Drained Triaxial (3x9)	Reconstituted Incremental Oedometer (16)
Anisotropically Consolidated Undrained Triaxial Compression (11)	Anisotropically Consolidated Undrained Triaxial Extension + Bender Element (5)	Constant Rate of Strain Oedometer (9)	Direct Simple Shear (17)
Anisotropically Consolidated Undrained Triaxial Compression + Bender Element (8)	Consolidated Cyclic Triaxial (4)	Incremental Oedometer (11)	Cyclic Simple Shear (15)

C Mudline Deformations

Table C-5 Mudline foundation displacements and rotations in sand, DLCs 6.1 and 3.2.

Load	Direction	D	d/D	Element Size	Nr of Elements	$\lvert u \rvert$	$\lvert u_x \rvert$	$\lvert u_z \rvert$	$\lvert \phi_y \rvert$
[-]	[-]	[m]	[-]	[m]	[-]	[m]	[m]	[m]	[°]
Storm	Clockwise	10	1.2	0.55	57780	0.063	0.062	-0.009	0.430
	Counter					0.060	-0.058	-0.015	-0.397
Production	Clockwise					0.058	0.057	-0.011	0.417
	Counter					0.055	-0.053	-0.017	-0.384
Storm	Clockwise	10	1.3	0.55	60062	0.055	0.054	-0.008	0.372
	Counter					0.053	-0.051	-0.015	-0.344
Production	Clockwise					0.050	0.049	-0.010	0.362
	Counter					0.049	-0.046	-0.016	-0.334
Storm	Clockwise	10	1.5	0.55	60607	0.043	0.043	-0.008	0.290
	Counter					0.043	-0.040	-0.015	-0.272
Production	Clockwise					0.040	0.038	-0.009	0.282
	Counter					0.040	-0.037	-0.016	-0.266
Storm	Clockwise	10	1.7	0.55	62864	0.034	0.033	-0.009	0.224
	Counter					0.037	-0.034	-0.015	-0.228
Production	Clockwise					0.031	0.030	-0.009	0.219
	Counter					0.034	-0.031	-0.016	-0.223
Storm	Clockwise	10	2.0	0.55	66747	0.025	0.023	-0.010	0.151
	Counter					0.031	-0.027	-0.015	-0.182
Production	Clockwise					0.023	0.020	-0.010	0.149
	Counter					0.029	-0.024	-0.016	-0.178

Table C-6 Mudline foundation displacements and rotations in clay, DLCs 6.1 and 3.2.

Load	Direction	D	d/D	Element Size	Nr of Elements	u	u_x	u_z	ϕ_y
[-]	[-]	[m]	[-]	[m]	[-]	[m]	[m]	[m]	[°]
Storm	Clockwise	10	1.2	0.55	57780	0.030	0.027	-0.013	0.207
	Counter					0.034	-0.030	-0.015	-0.232
Production	Clockwise					0.027	0.024	-0.013	0.212
	Counter					0.031	-0.027	-0.015	-0.237
Storm	Clockwise	10	1.3	0.55	60062	0.025	0.023	-0.011	0.172
	Counter					0.029	-0.025	-0.013	-0.192
Production	Clockwise					0.023	0.020	-0.011	0.177
	Counter					0.026	-0.022	-0.013	-0.196
Storm	Clockwise	10	1.5	0.55	60607	0.020	0.017	-0.009	0.128
	Counter					0.022	-0.019	-0.010	-0.141
Production	Clockwise					0.017	0.015	-0.009	0.131
	Counter					0.020	-0.017	-0.010	-0.144
Storm	Clockwise	10	1.7	0.55	60171	0.016	0.014	-0.008	0.097
	Counter					0.018	-0.015	-0.009	-0.111
Production	Clockwise					0.014	0.012	-0.008	0.099
	Counter					0.016	-0.013	-0.009	-0.112
Storm	Clockwise	10	2.0	0.55	66747	0.012	0.010	-0.006	0.067
	Counter					0.014	-0.012	-0.007	-0.081
Production	Clockwise					0.010	0.008	-0.006	0.069
	Counter					0.012	-0.010	-0.007	-0.082

D Effect of Load Level

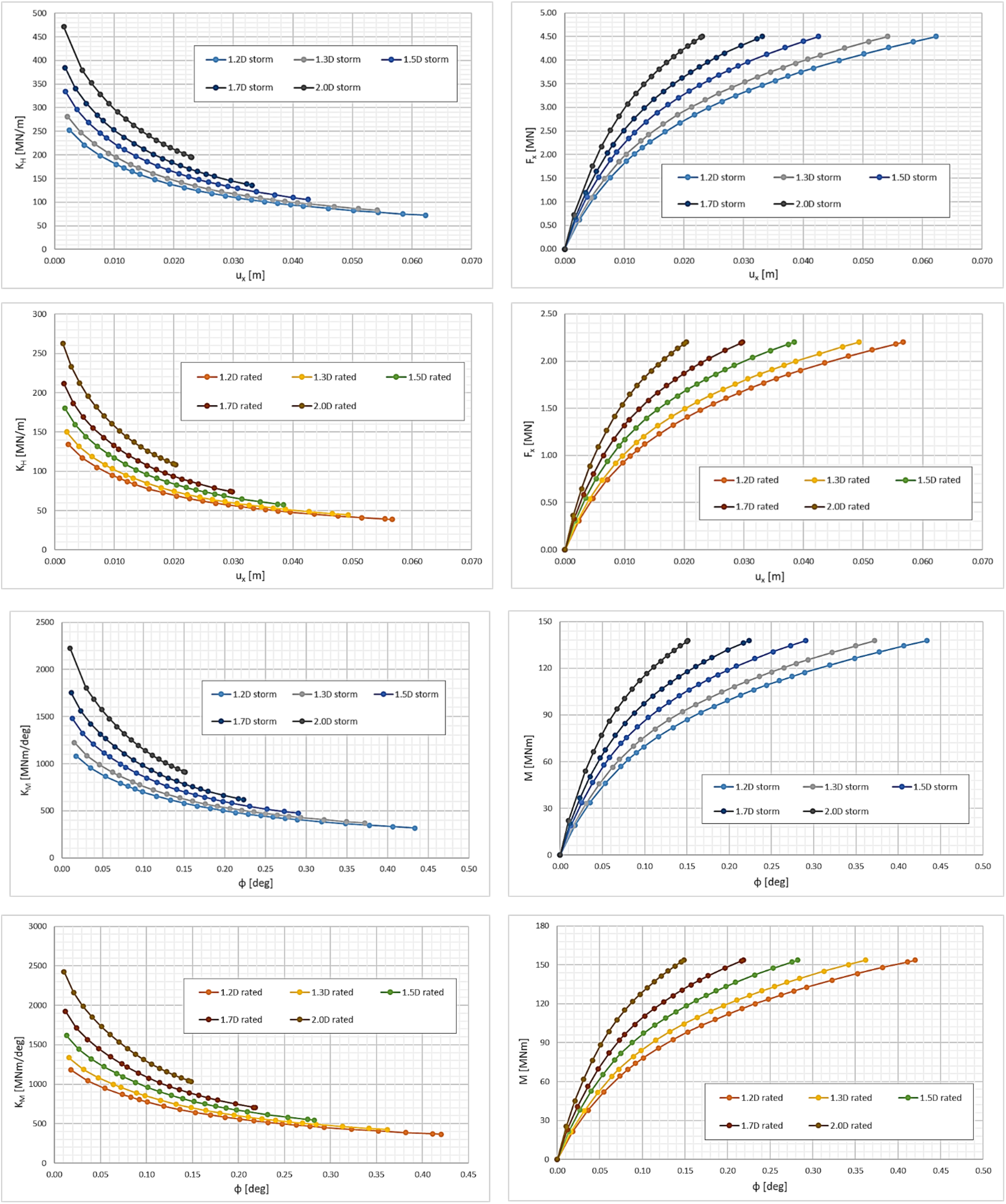

Figure D-1 Stiffness evolution and load-displacement curves in sand.

D Effect of Load Level

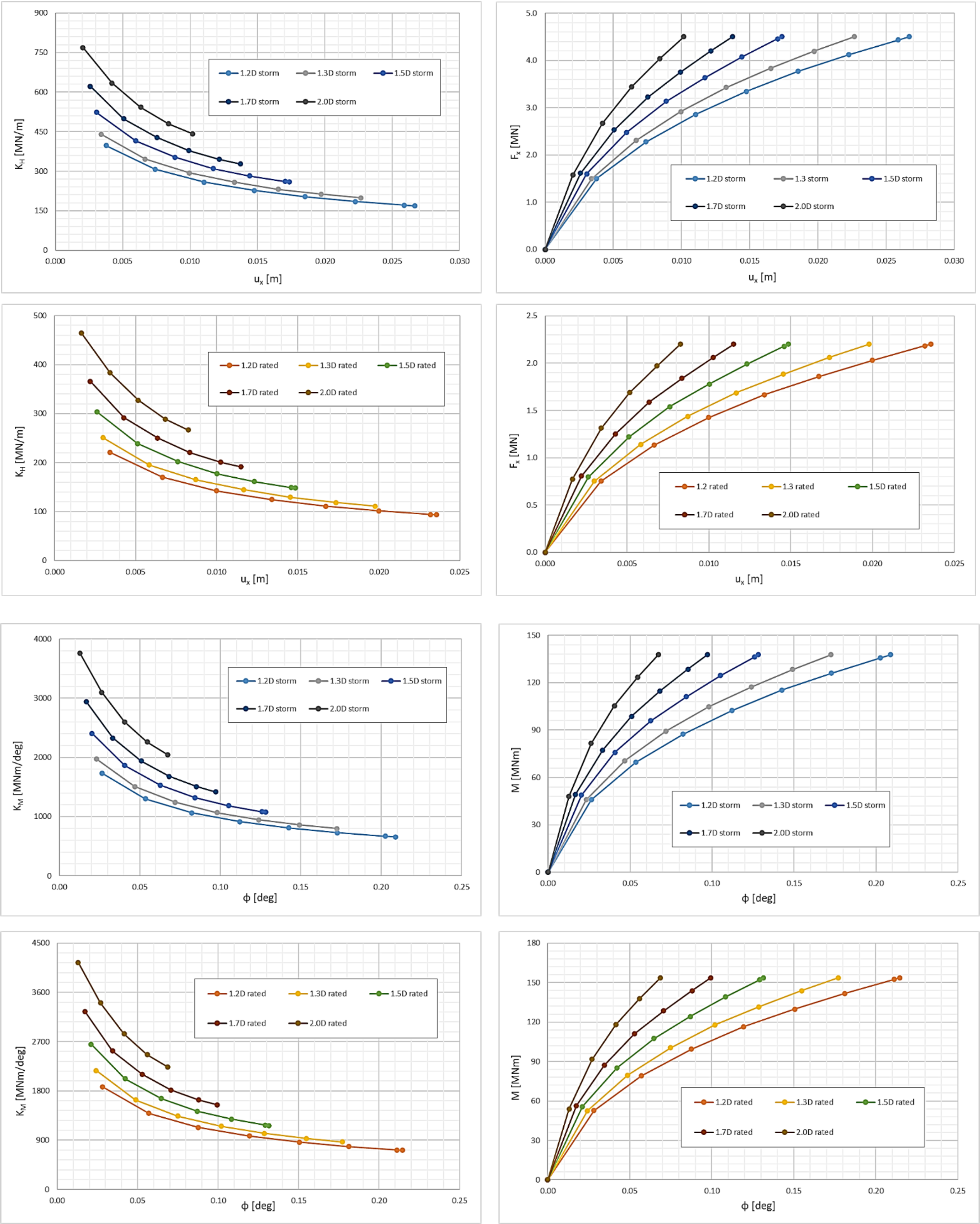

Figure D-2 Stiffness evolution and load-displacement curves in clay.

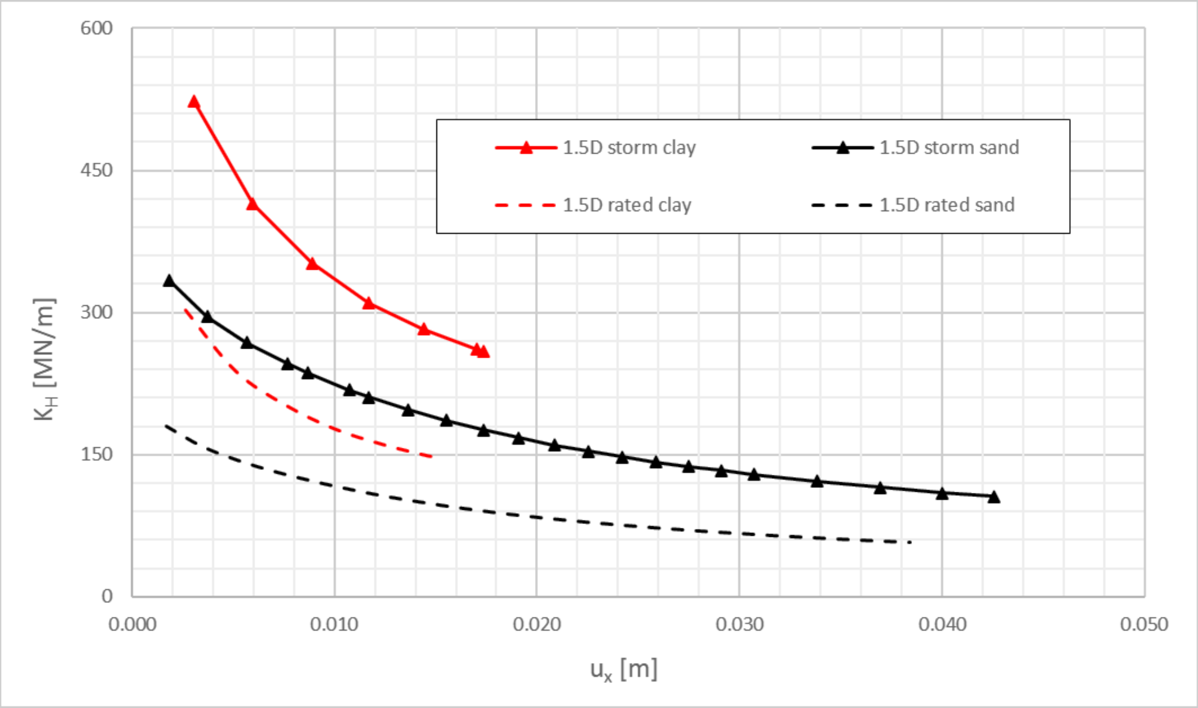

Figure D-3 Evolution of secant lateral foundation stiffness for DLCs 6.1 and 3.2 in sand and clay.

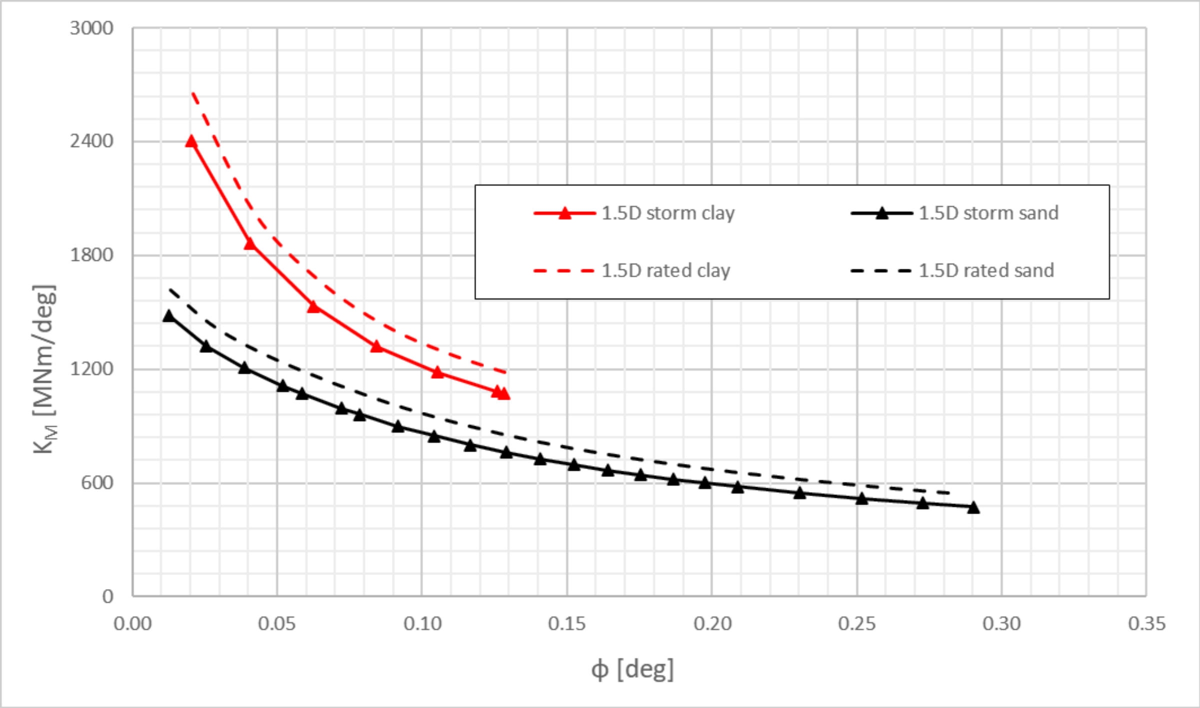

Figure D-4 Evolution of secant rotational foundation stiffness for DLCs 6.1 and 3.2 in sand and clay.

Bibliography

Ahmed, S. (2017). Enhancing the CPT correlation with the small strain shear stiffness of sands. *Ain Shams Engineering Journal*, 539-548.

Andersen, K. H., & Jostad, H. P. (2002). Shear Strength Along Outside Wall of Suction Anchors in Clay after Installation. *International Offshore and Polar Engineering Conference.* Kitakyushu, Japan.

Andersen, K. H., & Jostad, H. P. (2004). Shear Strength Along Inside of Suction Anchor Skirt Wall in Clay. *Offshore Technology Conference.* Houston, Texas.

Andersen, K., Murff, J., Randolph, M., Clukey, E., & Erbrich, C. (2005). Suction anchors for deepwater applications. *Frontiers in Offshore Geotechnics: Proceedings of the International Symposium. on Frontiers in Offshore Geotechnics.* Perth: Taylor & Francis.

Bentley. (2020). *Material Models Manual*. Retrieved from Bentley Communities: https://communities.bentley.com/products/geotech-analysis/w/plaxis-soilvision-wiki/46137/manuals---plaxis

BSH. (2021). *Reports on storm surges and extreme water levels*. Retrieved from Bundesamt für Seeschifffahrt und Hydrographie (BSH): https://www.bsh.de/EN/TOPICS/Water_levels_and_tides/Storm_surges/Storm_surges_node.html

Carbon Trust. (2015). Retrieved from Offshore wind industry review of Gravity Based Structures: https://www.carbontrust.com/resources/offshore-wind-industry-review-of-gravity-based-structures

Cathie, D., Jamie, I., Houlsby, G., Byrne, B., Buykx, S., Dekker, M., . . . Morgan, N. (2019). *Suction Installed Caisson Foundations for Offshore Wind: Design Guidelines.* Offshore Wind Accelerator.

Choo, Y., Kim, S., J., K., Lee, H., Kim, D., Youn, J., . . . Hossain, M. (2006). Centrifuge test of a clustered bucket foundation for offshore wind towers. In *ICPMG2014 – Physical Modelling in Geotechnics* (pp. 529-535). London: CRC Press.

Damiani, R., Dykes, K., & Scott, G. (2016). A comparison study of offshore wind support structures with monopiles and jackets for U.S. waters. *Journal of Physics: Conference Series 753*.

De Vos, L., Frigaard, P., & De Rouck, J. (2007). Wave run-up on cylindrical and cone-shaped foundations for offshore wind turbines. *Coastal Engineering 54*, 17-29.

Desmond, C., Murphy, J., Blonk, L., & Haans, W. (2016). Description of an 8 MW Reference Wind Turbine. *Journal of Physics: Conference Series 753:092013*.

DNV. (2016). *Design of Offshore Wind Turbine Structures.*

DNV GL. (2016). *Loads and site conditions for wind turbines.*

DNV GL. (2018). *Support structures for wind turbines.*

Empire Engineering. (2020, July). Retrieved from Foundation Ex: The Tech Session: How deep can the monopile go?

EOWDC. (2021). *Aberdeen (EOWDC) Offshore Wind Farm*. Retrieved from 4coffshore: https://www.4coffshore.com/windfarms/united-kingdom/aberdeen-(eowdc)-united-kingdom-uk47.html

ESMAP. (2021). Retrieved from Energy Sector Management Assistance Programme - Offshore Wind Technical Potential: https://esmap.org/esmap_offshorewind_techpotential_analysis_maps

Fugro. (2016). *Measured and Derived Geotechnical Parameters and Final Results, J11322-R-2, 29/07/2016.*

GE Renewable Energy. (2021). Retrieved from Haliade-X offshore wind turbine: https://www.ge.com/renewableenergy/wind-energy/offshore-wind/haliade-x-offshore-turbine

Holthuijsen, L. H. (2007). *Waves in Oceanic and Coastal Waters.* Cambridge: Cambridge University Press.

Houlsby, G. T., & Byrne, B. W. (2005a). Design procedures for installation of suction caissons in sand. *Geotechnical Engineering 158* (pp. 135-144). Proceedings of the Institution of Civil Engineers.

Houlsby, G. T., & Byrne, B. W. (2005b). Design procedures for installation of suction caissons in clay and other materials. *Geotechnical Engineering, 158*, 75-82.

Houlsby, G. T., Ibsen, L. B., & Byrne, B. W. (2005a). Suction caissons for wind turbines. *Frontiers in Offshore Geotechnics: Proceedings of the International Symposium. on Frontiers in Offshore Geotechnics (IS-FOG 2005)*, (pp. 75-92). Perth, WA, Australia.

Houlsby, G. T., Kelly, R. B., & Byrne, B. W. (2005b). The tensile capacity of suction caissons in sand under rapid loading. *Frontiers in Offshore Geotechnics: Proceedings of the International Symposium. on Frontiers in Offshore Geotechnics (IS-FOG 2005)* (pp. 405-410). Perth, WA, Australia: 19-21 Sept 2005.

Houlsby, G. T., Kelly, R. B., Huxtable, J., & Byrne, B. W. (2005c). Field trials of suction caissons in clay for offshore wind turbine foundations. *Geotechnique 55*, 287-296.

Houlsby, G. T., Kelly, R. B., Huxtable, J., & Byrne, B. W. (2006). Field trials of suction caissons in sand for offshore wind turbine foundations. *Géotechnique 56*, 3-10.

Hung, L. C., Lee, S., Tran, N. X., & Kim, S.-R. (2017). Experimental investigation of the vertical pullout cyclic response of bucket foundations in sand. *Applied Ocean Research, 68*, 325-335.

IEA. (2020). Retrieved from International Energy Agency: Renewables 2020 - Analysis and Forecast to 2025: https://iea.blob.core.windows.net/assets/1a24f1fe-c971-4c25-964a-57d0f31eb97b/Renewables_2020-PDF.pdf

IEC. (2005). *Wind turbines Part 1: Design requirements.*

IOC. (2021). *Intergovernmental Oceanographic Commission (IOC): Sea level station monitoring facility*. Retrieved from ioc-sealevelmonitoring: http://www.ioc-sealevelmonitoring.org/station.php?code=abed

IRENA. (2019). Retrieved from Future of Wind: https://www.irena.org/-/media/files/irena/agency/publication/2019/oct/irena_future_of_wind_2019.pdf

IRENA. (2021). Retrieved from International Renewable Energy Agency - Wind Energy Data: https://www.irena.org/wind

Karapiperis, K., & Gerolymos, N. (2014). Combined loading of caisson foundations in cohesive soil: Finite element versus Winkler modelling. *Computers and Geotechnics 56*, 100-120.

Kelly, R., T., H. G., & Byrne, B. W. (2006). A comparison of field and laboratory tests of caisson foundations in sand and clay. *Géotechnique 56*, 617-626.

Kim, D.-J., Choo, Y. W., Lee, J.-S., Kim, D.-S., Jee, S.-H., Choi, J., . . . Park, Y.-H. (2009). Numerical Analysis of Cluster and Monopod Suction Bucket Foundation. *ASME 2013 32nd International Conference on Ocean, Offshore and Arctic Engineering* (p. V006T10A022). Nantes, France: American Society of Mechanical Engineers.

Lambae, T. W., & Whitman, R. V. (1979). *Soil mechanics, SI version.* New York: John Wiley & Sons.

Liu, Y. E. (2021). *Overcoming the Technical Boundaries of Monopile Foundations in Deep Waters.* TU Delft.

Lozano-Minguez, E., Kolios, A., & Brennan, F. (2011). Multi-criteria assessment of offshore wind turbine support structures. *Elsevier: Renewable Energy*, 2831-2837.

Lunne, T., Eide, O., & Ruiter, J. d. (1976). Correlations between cone resistance and vane shear strength in some Scandinavian soft to medium stiff clays. *Canadian Geotechnical Journal, 13*, 430-441.

MingYang Smart Energy. (2021). Retrieved from MySE 16.0-242: http://www.myse.com.cn/en/jtxw/info.aspx?itemid=825

Mitchell, J. K. (1960). Fundamental Aspects of Thixotropy in Soils. *Journal of Soil Mechanics and Foundation Divisions ASCE, 86*, 19-53.

Mohammed, M., Messerman, A., Mayhan, B., & Trauth, K. (2016). Theory and Practice of the Hydrodynamic Redesign of Artificial Hellbender Habitat.

Mohd, Z., & Noor, I. (2013). Comparison of Extreme Responses From Wheeler and Vertical Stretching Methods. *Proceedings of the ASME 32nd International Conference on Ocean, Offshore and Arctic Engineering.* Nantes, France.

Mylonas-Rontiris, A. (2018). *Behaviour of isotropically and anisotropically consolidated kaolin clay under axisymmetric triaxial loading conditions*. Retrieved from DSpace NTUA: https://dspace.lib.ntua.gr/xmlui/handle/123456789/47690

OESEA3. (2016). *Appendix 1D: Water Environment*. Retrieved from UK OESEA 3: https://assets.publishing.service.gov.uk/government/uploads/system/uploads/attachment_data/file/504541/OESEA3_A1d_Water_environment.pdf

Offshore magazine. (2020). Retrieved from UK leading offshore wind jacket foundation trend: https://www.offshore-mag.com/field-development/article/14167727/uk-leading-offshore-wind-jacket-foundation-trend

offshoreWIND.biz. (2021, September). Retrieved from The Return of the Tripod: https://www.offshorewind.biz/2021/09/28/the-return-of-the-tripod-foundation-specialists-see-an-opening/

Oh, K.-Y., Nam, W., Ryu, M., Kim, J.-Y., & Epureanu, B. (2018). A review on the foundation of offshore wind energy converters: current status and future perspectives. *Elsevier: Renewable and Sustainable Energy Reviews*, 16-36.

Ramboll. (2018). *Engineering Report – Add. Design Checks for 8-8MW OPTI TIP Mode, 301000327/AOWF-514-032, 05/12/2018.*

Randolph, M., & Gourvenec, M. (2011). *Offshore geotechnical engineering.* CRC Press.

Robertson, P. (2009). Interpretation of cone penetration tests - a unified approach. *Canadian Geotechnical Journal, 46*(11), 1337-1355.

Robertson, P. K., & Campanella, R. G. (1983). Interpretation of Cone Penetration Tests. *Canadian Geotechnical Journal , 20*(4).

Siemens Gamesa. (2021). Retrieved from SG 14-222 DD Offshore wind turbine: https://www.siemensgamesa.com/products-and-services/offshore/wind-turbine-sg-14-222-dd

SPT Offshore. (2016). *Geotechnical Ground Model and Design Parameters, 20153051.DOC.101, 23/12/2016.*

SPT Offshore. (2017a). *Bucket Foundation Design Basis, 20153051.DOC.0103, 23/02/2017.*

SPT Offshore. (2017b). *Suction Bucket Foundation – Detailed Geotechnical Design, 20153051.DOC.0106, 21/07/2017.*

SPT Offshore. (2021). Retrieved from Wind Turbine Generator (WTG) foundations - Tri-suction Pile Caisson (TSPC): https://www.sptoffshore.com/wind-turbine-generator-wtg-foundations/

Sturm, H. (2017). Design Aspects of Suction Caissons for Offshore Wind Turbine Foundations. *Proceedings of TC 209 Workshop - 19th ICSMGE*, (pp. 45-63). Seoul.

Temple, G. (1952). The accuracy of Rayleigh's method of calculating the natural frequencies of vibrating systems. *Proceedings of the Royal Society of London. Series A. Mathematical and Physical Sciences*(211), 204-224.

US Department of Energy. (2021). Retrieved from Wind Market Report: 2021 Edition: https://www.energy.gov/sites/default/files/2021-08/Offshore%20Wind%20Market%20Report%202021%20Edition_Final.pdf

Vestas. (2011). *V164-8.0 MW*. Retrieved from Archiexpo: https://pdf.archiexpo.com/pdf/vestas/vestas-v164-80-mw/88087-134417-_6.html

Vestas. (2021). Retrieved from V236-15.0 MW: https://www.vestas.com/en/products/offshore%20platforms/v236_15_mw#!

Villalobos, F. A., Byrne, B. W., & Houlsby, G. T. (2009). An Experimental Study of the Drained Capacity of Suction Caisson Foundations Under Monotonic Loading For Offshore Applications. *Soils and Foundations 49*, 477-488.

Vries, E. d. (2013). *Close up - Vestas V164-8.0 nacelle and hub*. Retrieved from Windpower Monthly: https://www.windpowermonthly.com/article/1211056/close-vestas-v164-80-nacelle-hub

Wandji, W. N., Natarajan, A., Dimitrov, N., & Buhl, T. (2015). Design of monopiles for multi-megawatt wind turbines at 50 m water depth. *European Wind Energy Association Annual Conference and Exhibition 2015, EWEA 2015 - Scientific*.

Wang, X., Zeng, X., & Li, J. (2019). Vertical performance of suction bucket foundation for offshore wind turbines in sand. *Ocean Engineering*, 40-48.

WindEurope. (2019). Retrieved from Key trends and statistics: https://windeurope.org/wp-content/uploads/files/about-wind/statistics/WindEurope-Annual-Offshore-Statistics-2019.pdf